Contents lists available at ScienceDirect

International Journal of Applied Earth Observation and Geoinformation

journal homepage: www.elsevier.com/locate/jag

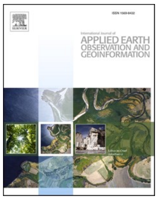

Improving the accuracy of SIF quantified from moderate spectral resolution airborne hyperspectral imager using SCOPE: assessment with sub-nanometer imagery

A. Belwalkar [a,*], T. Poblete [a,b], A. Hornero [a,c], R. Hernández-Clemente [d,e], P.J. Zarco–Tejada [a,b,c]

[a] Department of Infrastructure Engineering, Faculty of Engineering and Information Technology (FEIT), The University of Melbourne, Melbourne, Victoria, Australia
[b] School of Agriculture, Food and Ecosystem Sciences (SAFES), Faculty of Science (FoS), The University of Melbourne, Melbourne, Victoria, Australia
[c] Instituto de Agricultura Sostenible (IAS), Consejo Superior de Investigaciones Científicas (CSIC), Avenida Menéndez Pidal s/n, 14004 Córdoba, Spain
[d] Department of Geography, Swansea University, SA2 8PP Swansea, United Kingdom
[e] Departamento de Ingeniería Forestal, Universidad de Córdoba, Campus de Rabanales, Crta, IV, km. 396, E-14071 Córdoba, Spain

ARTICLE INFO

Keywords:
Solar-induced chlorophyll fluorescence
SIF
Narrow-band
SCOPE
Airborne
Hyperspectral
Hyperspectral imaging

ABSTRACT

Hyperspectral imaging of solar-induced chlorophyll fluorescence (SIF) is required for plant phenotyping and stress detection. However, the most accurate instruments for SIF quantification, such as sub-nanometer ($\leq$1-nm full-width at half-maximum, FWHM) airborne hyperspectral imagers, are expensive and uncommon. Previous studies have demonstrated that standard narrow-band hyperspectral imagers (i.e., 4–6-nm FWHM) are more cost-effective and can provide far-red SIF quantified at 760 nm (SIF_{760}), which correlates strongly with precise sub-nanometer resolution measurements. Nevertheless, narrow-band SIF_{760} quantifications are subject to systematic overestimation owing to the influence of the spectral resolution (SR). In this study, we propose a modelling approach based on the Soil Canopy Observation, Photochemistry and Energy Fluxes (SCOPE) model with the objective of enhancing the accuracy of absolute SIF_{760} levels derived from standard airborne hyperspectral imagers in practical settings. The performance of the proposed method was evaluated using airborne imagery acquired from two airborne hyperspectral imagers (FWHM $\leq$ 0.2-nm and 5.8-nm) flown in tandem on board an aircraft that collected data from two different wheat and maize phenotyping trials. Leaf biophysical and biochemical traits were first estimated from airborne narrow-band reflectance imagery and subsequently used as SCOPE model inputs to simulate a range of top-of-canopy (TOC) radiance and SIF spectra at 1-nm FWHM. The SCOPE simulated radiance spectra were then convolved to match the spectral configuration of the narrow-band imager to compute the 5.8-nm FWHM SIF_{760}. A site-specific model was constructed by employing the convolved 5.8-nm SR SIF_{760} as the independent variable and the 1-nm SR SIF_{760} directly simulated by SCOPE as the dependent variable. When applied to the airborne dataset, the estimated SIF_{760} at 1-nm SR from the standard narrow-band hyperspectral imager matched the reference sub-nanometer quantified SIF_{760} with root mean square error (RMSE) less than 0.5 mW/m^2/nm/sr, yielding R^2 = 0.93–0.95 from the two experiments. These results suggest that the proposed modelling approach enables the interpretation of SIF_{760} quantified using standard hyperspectral imagers of 4–6 nm FWHM for stress detection and plant physiological condition assessment.

1. Introduction

Solar-induced chlorophyll fluorescence (SIF) is a weak electromagnetic signal emitted by chlorophyll *a* that provides useful information about plant photosynthetic activity and stress (Lichtenthaler and Rinderle, 1988; Campbell et al., 2008; Zarco-Tejada et al., 2021). Direct measurement of the SIF signal is complex due to its superimposition on the reflected solar radiation and small magnitude (1–5 % of total upwelling radiance in the near infrared) (Meroni et al., 2009). Since sensor capabilities impact the shape of absorption features commonly used for SIF quantification, instruments with sufficient spectral resolution (SR) and signal-to-noise ratio (SNR) are required for detecting subtle

---

* Corresponding author.
E-mail address: anirudhb.099@gmail.com (A. Belwalkar).

https://doi.org/10.1016/j.jag.2024.104198
Received 26 July 2024; Received in revised form 16 September 2024; Accepted 1 October 2024

variations across narrow absorption features for accurate SIF quantification (Mohammed et al., 2019). Sensors with a sub-nanometer resolution are thus recommended for quantifying SIF in precise physical units and absolute terms.

SIF signal can be retrieved using a range of platforms, including ground-based spectrometers (Cogliati et al., 2015; Hao et al., 2022; Li et al., 2020), drones (Chang et al., 2020; Suarez et al., 2021; N. Wang et al., 2021; Zarco-Tejada et al., 2012), piloted aircrafts (Damm et al., 2015; 2022; Poblete et al., 2020; Rascher et al., 2015), and satellites (Braghiere et al., 2021; Köhler et al., 2018; Sun et al., 2018). Airborne platforms serve as an intermediary scale between field and satellite SIF quantifications, enabling a more precise and localised evaluation of vegetation health and dynamics, which is particularly critical for heterogeneous landscapes. Furthermore, the temporal control provided by airborne platforms in terms of data gathering throughout crucial growth stages, as well as the capability for multi-sensor integration, allows for a more comprehensive understanding of the factors influencing plant physiological state. For airborne SIF quantification, there are several imaging sensors with sub-nanometer resolution capabilities, such as the chlorophyll fluorescence imaging spectrometer (CFIS) (Frankenberg et al., 2018), the high-resolution airborne imaging spectrometer HyPlant (Rascher et al., 2015), the AISA IBIS Fluorescence Imager (SPECIM, Spectral Imaging Ltd., Oulu, Finland) (R. Wang et al., 2022), and the Hyperspec Solar-Induced Fluorescence Imaging sensor (Headwall Photonics, Fitchburg, MA, USA) (Belwalkar et al., 2022) with SRs of 0.07, 0.28, 0.245, and ≤0.2 nm, respectively. These sub-nanometer imaging sensors can precisely characterise narrow absorption features needed for the accurate quantification of SIF in physical units.

Despite their potential, sub-nanometer imaging sensors pose significant challenges that restrict their widespread use for plant physiology monitoring, precision agriculture, and plant phenotyping applications. Their radiometric calibration is among the most challenging aspects. Since these sensors have narrow contiguous bands with a spectral sampling interval (SSI) on the order of 10^{-1} nm, a sophisticated calibration facility is required for accurate characterisation of the detector's spectral response (Brown et al., 2006). The challenge of handling multiple flight lines presents an additional obstacle, primarily due to the substantial volume of data generated from a large number of bands, typically exceeding 1000 bands, as reported in Rascher et al. (2015) and Belwalkar et al. (2022). This vast volume of data complicates the process of creating a mosaic from numerous flight lines. Furthermore, these sensors have a spectral range limited to the SIF emission region (650–800 nm). Consequently, they cannot be used to simultaneously estimate plant traits, vegetation indices, and quantify SIF, necessitating the integration of an additional sensor into the airborne platform. In addition, their weights make these sensors incompatible with drones, requiring lightweight aircraft to be used as the aerial platform (Frankenberg et al., 2018; Headwall Photonics, 2023; Specim, 2022).

In recent years, there has been rapid progress in the use of hyperspectral imaging sensors with narrow-band SRs in the 4–6-nm FWHM range, in conjunction with drones and lightweight aircraft (Aasen et al., 2018). A variety of compact, lightweight, and low-cost narrow-band hyperspectral imaging sensors in the visible and near-infrared spectral range (400–1000 nm) are now widely available, such as Specim AFX10 (5.5-nm FWHM, SPECIM, Spectral Imaging Ltd., Oulu, Finland), Micro- and Nano-Hyperspec (5.8- and 6-nm FWHM, respectively, Headwall Photonics Inc., Boston, MA, USA), Pika L and Pika XC2 (3.3- and 1.9-nm FWHM, respectively, Resonon Inc., Bozeman, MT, USA), and FireflEYE 185 (8-nm FWHM, Cubert GmbH, Ulm, Baden-Württemberg, Germany), among others. These sensors have the capability of retrieving narrow-band hyperspectral vegetation indices and estimating numerous plant functional traits, which could provide substantial insight into the health of the plant. Furthermore, these sensors can be mounted on either piloted or non-piloted airborne platforms. These standard narrow-band hyperspectral imagers could provide a cost-effective and more operationally viable alternative to sub-nanometer imagers for quantifying far-red SIF at 760 nm, hereafter SIF_{760}. Several past studies have demonstrated the utility of relative SIF_{760} levels derived from standard narrow-band imaging sensors for a variety of applications, such as biotic-induced stress detection (Calderón et al., 2013; Hernández-Clemente et al., 2017; Hornero et al., 2021; Poblete et al., 2021; 2020; Zarco-Tejada et al., 2021; 2018), water stress detection (Camino et al., 2018a; Panigada et al., 2014; Zarco-Tejada et al., 2012), plant phenotyping (Camino et al., 2019; 2018b; Gonzalez-Dugo et al., 2015), nutrient assessment (Longmire et al., 2022; Y. Wang et al., 2022; Watt et al., 2020) and its link with gross primary production (GPP) (Damm et al., 2015; Zarco-Tejada et al., 2013). More recently, Belwalkar et al. (2022) found strong correlations between airborne SIF_{760} quantified from a narrow-band hyperspectral imager with 5.8-nm FWHM and sub-nanometer SIF_{760} acquired concurrently using an airborne sub-nanometer hyperspectral imager with ≤0.2-nm FWHM and a ground-based spectrometer with 0.065-nm FWHM. Although narrow-band quantified SIF_{760} were larger than sub-nanometer quantified SIF_{760} (root mean square error, RMSE = 3.28–4.69 $\text{mW/m}^2\text{/nm/sr}$), SIF_{760} levels quantified from both airborne sensors were strongly correlated ($R^2 = 0.77$–0.9) across multiple experimental sites. Thus, we hypothesise that spectrally scaling narrow-band SIF_{760} imaging to finer resolutions using physically-based models could facilitate the quantification of absolute SIF_{760} levels at finer spatial resolutions.

Due to the re-absorption and scattering of light within the leaves and canopy, plant pigments and canopy structure have strong effects on top-of-canopy (TOC) SIF (Dechant et al., 2020; Porcar-Castell et al., 2014; Van der Tol et al., 2016; Yang and Van der Tol, 2018; Zeng et al., 2019). Previous studies utilising physically-based models successfully accounted for these light re-absorption and scattering effects when downscaling SIF from the canopy level to the leaf level (Liu et al., 2019; Romero et al., 2020; Yang and Van der Tol, 2018). In addition, prior studies have demonstrated that SIF spectra and vegetation biophysical and biochemical traits can be retrieved simultaneously, either with radiative transfer model (RTM) inversion alone (Celesti et al., 2018; Verhoef et al., 2018) or through RTM combined with machine learning modelling (Scodellaro et al., 2022). The widely used RTM Soil-Canopy-Observation of Photosynthesis and Energy fluxes (SCOPE) (Van der Tol et al., 2009) can model light re-absorption and scattering mechanisms within leaves and canopies while taking canopy structure into consideration. Several recent studies (Wang et al., 2023; Wieneke et al., 2024; Wu et al., 2024) have illustrated the potential of the SCOPE model for the modelling of canopy fluorescence. A sensitivity analysis of the SCOPE model revealed that canopy structure and leaf optical properties primarily determine TOC SIF variability when considering only vegetation parameters (Verrelst et al., 2015). Consequently, the interpretation of narrow-band quantified SIF_{760} could be improved by including plant trait information derived from RTMs, such as SCOPE. We hypothesise that incorporating plant trait information through the SCOPE-based modelling approach could potentially aid in the quantification of SIF_{760} at finer spectral resolution from standard narrow-band resolution sensors, enabling retrieval of appropriate absolute SIF_{760} levels in physical units.

Although Belwalkar et al. (2022) demonstrated significant correlations between SIF_{760} quantifications derived from narrow-band and sub-nanometer airborne hyperspectral imagers flown in tandem, these narrow-band SIF_{760} quantifications were accurate only in relative terms, and their conversion to absolute SIF_{760} levels in physical units required further investigation. Furthermore, several prior studies have demonstrated that sensors with broader spectral specifications overestimate SIF_{760} (Damm et al., 2015; Julitta et al., 2016; Maimaitiyiming et al., 2020; Nichol et al., 2019). Damm et al. (2011) demonstrated that the magnitude of this bias is predominantly influenced by SNR of the instrument, with SR (≤40 %), SSI (≤12 %), and spectral shift (SS) (≤7%) accounting for the remaining errors, respectively. These results highlight the need for further modelling efforts for accurate SIF quantification in practical applications. Although previous studies have demonstrated the impact of the spectral resolution on SIF (Cendrero-

Mateo et al., 2019; Damm et al., 2011; Julitta et al., 2016; Liu et al., 2015), they have mostly focused on modelling efforts and on hand-held spectrometer data collected at the near-field scale. There is a lack of research focusing on assessing the impact of sensor spectral characteristics on SIF from standard narrow-band imaging sensors under ambient field conditions. Studies carried out under such conditions with operational sensors will make progress on the operational use of cost-efficient and simpler sensors for fluorescence quantification and photosynthesis assessment.

Our study extends the prior work of Belwalkar et al. (2022) by modelling the effect of SR on airborne SIF_{760} quantified by standard hyperspectral imagers of 4–6 nm FWHM to optimise their interpretation, with the intention of addressing the limitations associated with the bias observed when looking at the absolute SIF_{760} levels quantified from standard airborne hyperspectral imagers in practical applications. Using airborne SIF_{760} data obtained from a standard hyperspectral imager with a 5.8-nm FWHM resolution over plant phenotyping trials as input, we developed a model based on SCOPE to estimate airborne SIF_{760} at a finer target resolution. Due to SCOPE's default spectral characteristics and previous experimental results indicating that spectrometers with FWHM $\leq$1-nm can estimate the absolute value of SIF_{760} (Julitta et al., 2016), we selected 1-nm FWHM as the target resolution for validation purposes.

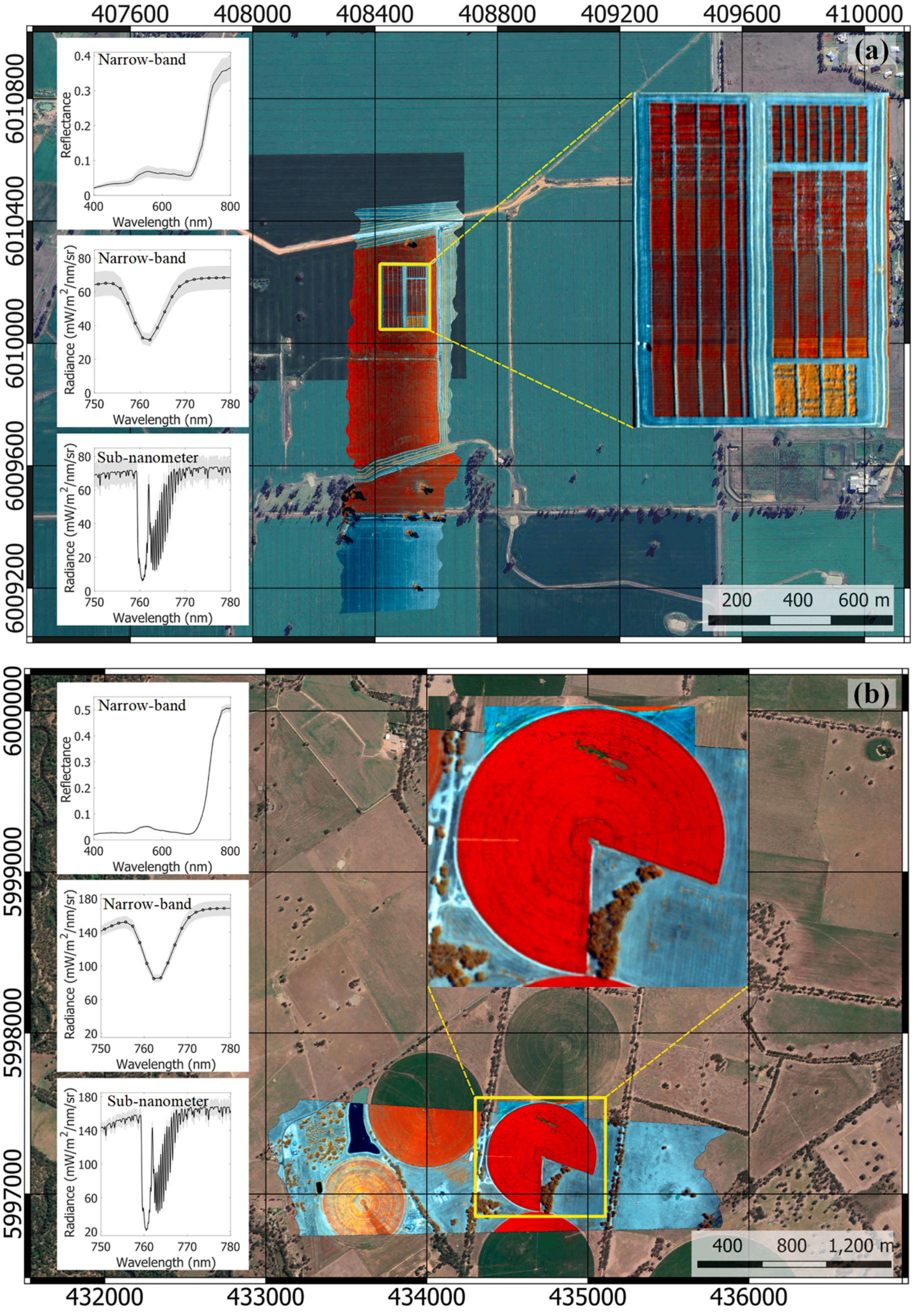

Fig. 1. Overview of experimental fields at Sites 1 (a) and 2 (b) acquired with the narrow-band hyperspectral imager (composite: 760 (R), 710 (G), and 680 (B) nm). The black lines correspond to the average radiance spectra in the O_2-A absorption region used for SIF quantification and the average reflectance spectra in the 400–800-nm spectral region used for plant trait estimation for all plots. Shaded areas in the reflectance and radiance plots represent the ±1 standard deviation of the average reflectance and radiance. The background maps depict Google Maps Satellite imagery.

2. Materials and methods

2.1. Study sites

The study was conducted at two sites in Victoria, Australia (Fig. 1). Site 1 was located in Yarrawonga (36°02'55"S, 145°59'02") and was planted with several varieties of rainfed wheat grown under various physiological conditions and fertilisation treatments. The airborne campaign was conducted during grain filling in 2019 (Fig. 1a). Plots were 26 m^2 (2 m × 13 m) in size and were planted in May 2019. The second trial site (Site 2) was managed under irrigated conditions using an overhead pivot in Peechelba East (36°10'04″S, 146°16'23″E) in 2021. A single variety of maize (Pioneer Hybrid 1756) was grown across the entire experimental field under different nitrogen fertiliser application rates. The growth stage during the airborne campaign corresponded to silking (Fig. 1b). Plots measured 36 m^2 (3 m × 12 m) and were planted in October 2020. The application of different nitrogen fertilisation treatments at both study sites resulted in a range of nutrient deficiency and stress levels.

At both trial sites, leaf measurements were carried out in the field simultaneously with airborne campaigns. Handheld leaf-clip sensors (Dualex, FORCE-A, Orsay, France and FluorPen FP110-LM, Photon Systems Instruments, Drásov, Czech Republic) were used to measure leaf chlorophyll content, nitrogen balance index (NBI), flavonol content, anthocyanin content, and steady-state leaf fluorescence yield (F_t). Details of leaf-level measurements can be found in Belwalkar et al. (2022). A portable weather station (model WXT510, Vaisala, Helsinki, Finland) was set up for concurrent readings of meteorological conditions (air temperature and air pressure) during the hyperspectral image acquisition over both of the trial sites. The total incoming irradiance (E) was measured continuously during flights with a 0.065-nm FWHM HR-2000 spectrometer (Ocean Insight, Dunedin, FL, USA) set up at each field site. The spectrometer at Site 1 was equipped with a CC-3 VIS-NIR cosine corrector-diffuser probe, whereas at Site 2, irradiance was measured using the radiance (L) reflected from a white reference panel (Labsphere Inc., North Sutton, NH, USA). The irradiance measured from the HR-2000 spectrometer was calibrated using coefficients derived from a uniform calibrated light source and an integrating sphere (Labsphere XTH2000C, Labsphere Inc., North Sutton, NH, USA).

2.2. Hyperspectral airborne campaigns

For both airborne campaigns, two hyperspectral imagers were flown in tandem on a Cessna 172R aircraft operated by the HyperSens Laboratory, the University of Melbourne's Airborne Remote Sensing Facility, to acquire high-resolution hyperspectral imagery over the two study sites. The first hyperspectral imager (Hyperspec VNIR E-Series model, Headwall Photonics, Fitchburg, MA, USA) captured images in the 400–1000-nm spectral range with 5.8-nm FWHM resolution, and the second hyperspectral imager (Hyperspec Solar-Induced Fluorescence Imaging sensor, Headwall Photonics, Fitchburg, MA, USA) operated in the 670–780-nm spectral range with ≤0.2-nm FWHM resolution. Further technical details of the imaging and flight data can be found in Tables 1 and 2.

The radiometric calibration of the two hyperspectral imagers was performed by means of an integrating sphere (Labsphere XTH2000C) using coefficients derived from the calibrated light source at four different illumination levels. We used the MODerate resolution atmospheric TRANsmission (MODTRAN) model (Berk et al., 2014) to perform atmospheric correction for the VNIR E-Series (narrow-band) imager to convert radiance images to reflectance images. Aerosol optical depth measurements in the 440-, 500-, 675-, 870-, and 936-nm spectral bands obtained from a Microtops II sun photometer (Solar Light Co., Philadelphia, PA, USA) and meteorological measurements from the portable weather station were used for input parameters. Hyperspectral images were *ortho*-rectified using inertial measurement units and GPS data (VN-300-VectorNav Technologies LLC, Dallas, TX, USA for the narrow-band imager and Trimble APX-15 UAV, Applanix Corporation, Ontario, Canada for the sub-nanometer imager) recorded during the flights using the Parametric Geocoding & Ortho-rectification for Airborne Optical Scanner Data software (PARGE, ReSe Applications Schläpfer, Wil, Switzerland). Additional information on data pre-processing and image correction can be found in Zarco-Tejada et al. (2016).

Table 1
Spectral characteristics of hyperspectral imagers.

	VNIR E-Series (Narrow-band)	**Solar-Induced Fluorescence Imaging (Sub-nanometer)**
Spectral range	400–1000 nm	670–780 nm
Number of spectral bands	371	2160
Spectral sampling interval (SSI)	1.626 nm	0.051 nm
FWHM	5.8-nm	≤0.2-nm
Number of un-binned spatial pixels	1600	1600
Signal-to-noise ratio (SNR)	>300:1*	>300:1*
Field of view	66°	23.5°

* Applicable only for plot-level mean radiance/reflectance computation.

Table 2
Details regarding hyperspectral image acquisition.

	Site 1	**Site 2**
Acquisition dates	9th October 2019, 15:40 – 16:30 (local time)	20th January 2021, 11:40 – 12:20 (local time)
Flight altitude (above ground level)	400 m (VNIR imager) 900 m (Fluorescence imager)	1200 m (both imagers)
Mean spatial resolution	0.2 m (both imagers)	0.7 m (VNIR imager) 0.3 m (Fluorescence imager)

We used the normalised difference vegetation index (NDVI) as a thresholding strategy to identify vegetational pixels within each plot, as described in Belwalkar et al. (2022). Mean radiance from both narrow-band and sub-nanometer imagers and reflectance spectra from the narrow-band imager were calculated for each plot by averaging all selected vegetation pixels, excluding the boundary pixels (Belwalkar et al., 2022). Differences in radiance spectra corresponding to the selected validation plots acquired from the two hyperspectral imagers were visually identified as a function of fertilisation treatments (Fig. 2). The average radiance spectra from the narrow-band hyperspectral imager (Fig. 2a and b) were used to quantify SIF_{760} using the O_2-A band *in-filling* approach, employing the Fraunhofer Line Depth (FLD) principle (Plascyk, 1975) and a total of three spectral bands (3FLD) (Maier *et al.*, 2003), named here as $SIF_{760\text{-}3FLD}$. The irradiance measured from HR-2000 spectrometer was convolved assuming a Gaussian band spectral response function of 5.8-nm FWHM resolution to match the spectral characteristics of the narrow-band hyperspectral imager. The '*in*' E and L were selected as the E/L minima in the 755–765-nm spectral region, while the '*out*' E and L were selected as the weighted mean of E/L local maxima in the 750–759-nm and 771–780-nm spectral regions, respectively. When applied at the pixel scale, the selection of exact minima and maxima is likely to be impacted by noise. However, in the current study, the 3FLD approach was not applied at the pixel scale, but rather at a plot-scale on mean narrow-band radiance spectra derived by spatial aggregation, thereby reducing the noise levels. In case of multiple local maxima within the spectral regions, the local maximum closest to the '*in*' band was selected (Cendrero-Mateo et al., 2019). The airborne $SIF_{760\text{-}3FLD}$ was further corrected using non-fluorescent soil targets

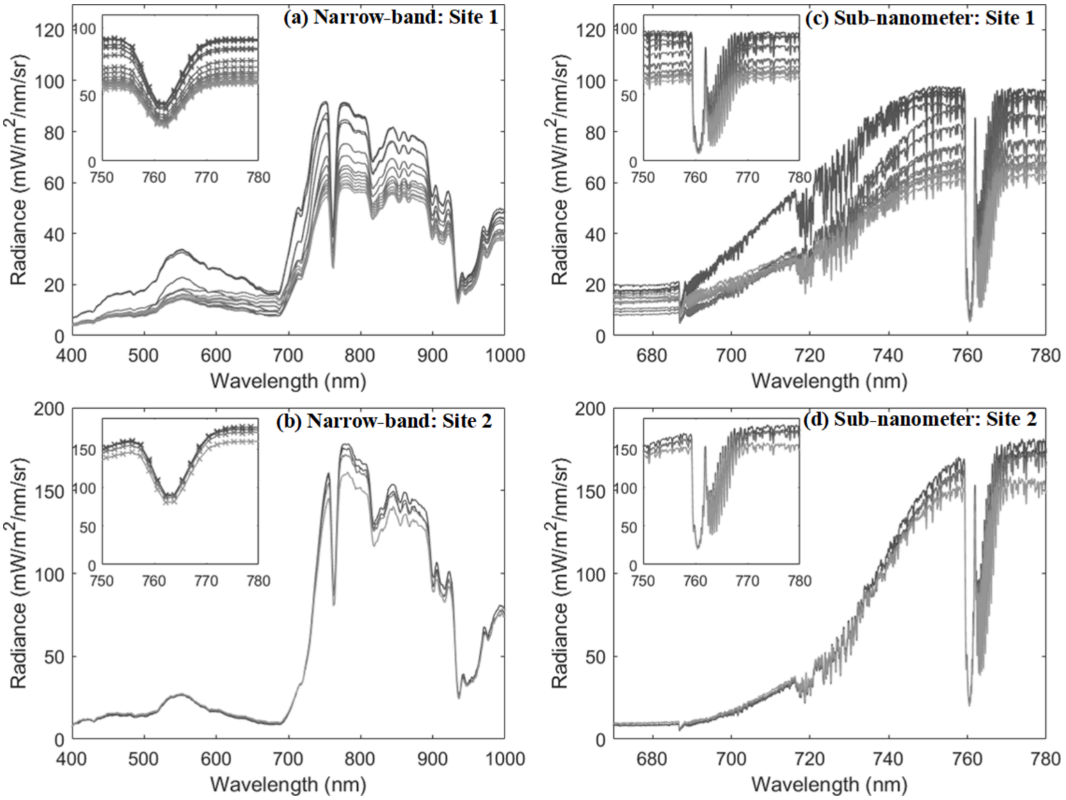

Fig. 2. Average plot-level radiance spectra obtained from narrow-band (a, b) and sub-nanometer imager (c, d) showing the variability across the selected validation plots at the two study sites due to different nitrogen treatments. The inset shows the O_2-A absorption feature in the 750- to 780-nm region.

identified in the imagery and then normalised using a reflectance-based angular normalisation approach (Hao et al., 2021) to account for atmospheric and directional effects as described in Belwalkar et al. (2022).

2.3. Modelling methods

2.3.1. Theoretical assessment of spectral resolution effects on SIF_{760} quantification using SCOPE

The SCOPE model (version 2.0) (Yang et al., 2021) was used to account for the effect of the sensor's spectral resolution on SIF_{760} quantification. A local sensitivity analysis was used to investigate how individual plant traits and fluorescence emission efficiency (ϵ_F) independently affect $SIF_{760\text{-}3FLD}$ quantifications from narrow-band hyperspectral imager used in this study. This differs from previous modelling-based studies (Damm et al., 2011; Liu et al., 2015) that varied multiple plant traits simultaneously. In simulations for Stage 1, the plant traits: leaf chlorophyll content (C_{a+b}), leaf area index (LAI), and leaf inclination distribution function ($LIDF_a$) were selected for analysis based on their association with SIF variability in a global SCOPE-sensitivity study (Verrelst et al., 2015). SCOPE simulations at the default 1-nm FWHM and 1-nm SSI were generated by randomly varying input parameters drawn from a uniform distribution within the following ranges: C_{a+b} (10–50 μg/cm^2), LAI (1–5 m^2/m^2), $LIDF_a$ (−0.8–0.8), and ϵ_F (0.01–0.03). A total of 1000 simulations were obtained for each trait while remaining SCOPE input parameters were set at their default values. SCOPE simulations were then convolved to match the SR, SSI, and band centres of the narrow-band hyperspectral imager, assuming a Gaussian band spectral response function. $SIF_{760\text{-}3FLD}$ was quantified from simulated irradiance and TOC total upwelling radiance at 5.8-nm FWHM resolution following the same methodology outlined in Section 2.2, and then compared to SIF_{760} directly simulated by SCOPE model at default 1-nm FWHM ($SIF_{760\text{-simulated}}$) across simulations. The outcome of local sensitivity analysis would provide insight into the relative influence of the most significant SCOPE parameters on absolute SIF_{760}, as quantified by a coarser resolution sensor.

2.3.2. SIF_{760} estimation at 1-nm FWHM from narrow-band hyperspectral imager

As summarised in Fig. 3, we first estimated plant traits from the narrow-band imager-derived mean airborne reflectance spectra obtained from each plot. Keeping ϵ_F fixed, we then utilised the estimated plant traits to model TOC SIF using the SCOPE model in forward mode. The SCOPE simulated spectra at the default 1-nm FWHM were convolved to match the spectral configuration of the narrow-band imager, enabling the computation of 5.8-nm FWHM $SIF_{760\text{-}3FLD}$. Subsequently, 5.8-nm FWHM $SIF_{760\text{-}3FLD}$ was utilised in conjunction with SCOPE simulated 1-nm FWHM SIF_{760} to develop a prediction model for estimating SIF_{760} at 1-nm FWHM. The prediction model was then applied to the narrow-band imager derived 5.8-nm FWHM $SIF_{760\text{-}3FLD}$ and the estimated airborne SIF_{760} at 1-nm FWHM was compared to sub-nanometer imager derived reference SIF_{760} at 1-nm FWHM.

The optical radiative transfer routine of the SCOPE model (RTMo) was used to invert the TOC reflectance spectra from the narrow-band imagery for biophysical and biochemical traits. Numerical Optimisation (NO) (Van der Tol et al., 2016; Yang et al., 2019) was used in the model inversion procedure to minimise a cost function estimating the differences between the observed and modelled TOC reflectance in the 400–800 nm spectral region. NO iteratively executes the RTMo model, implementing minor modifications to the free parameters within their permissible range (as specified in Table 3), until the cost function is minimised. Due to variations in meteorological conditions, crop type, and irrigation regime between the two study sites, distinct ranges and initial values were selected for specific traits. The estimated biophysical and biochemical traits were: leaf chlorophyll concentration (C_{a+b}), leaf carotenoid concentration (C_{ca}), leaf anthocyanin concentration (C_{ant}), leaf dry matter concentration (C_{dm}), leaf water concentration (C_w), leaf

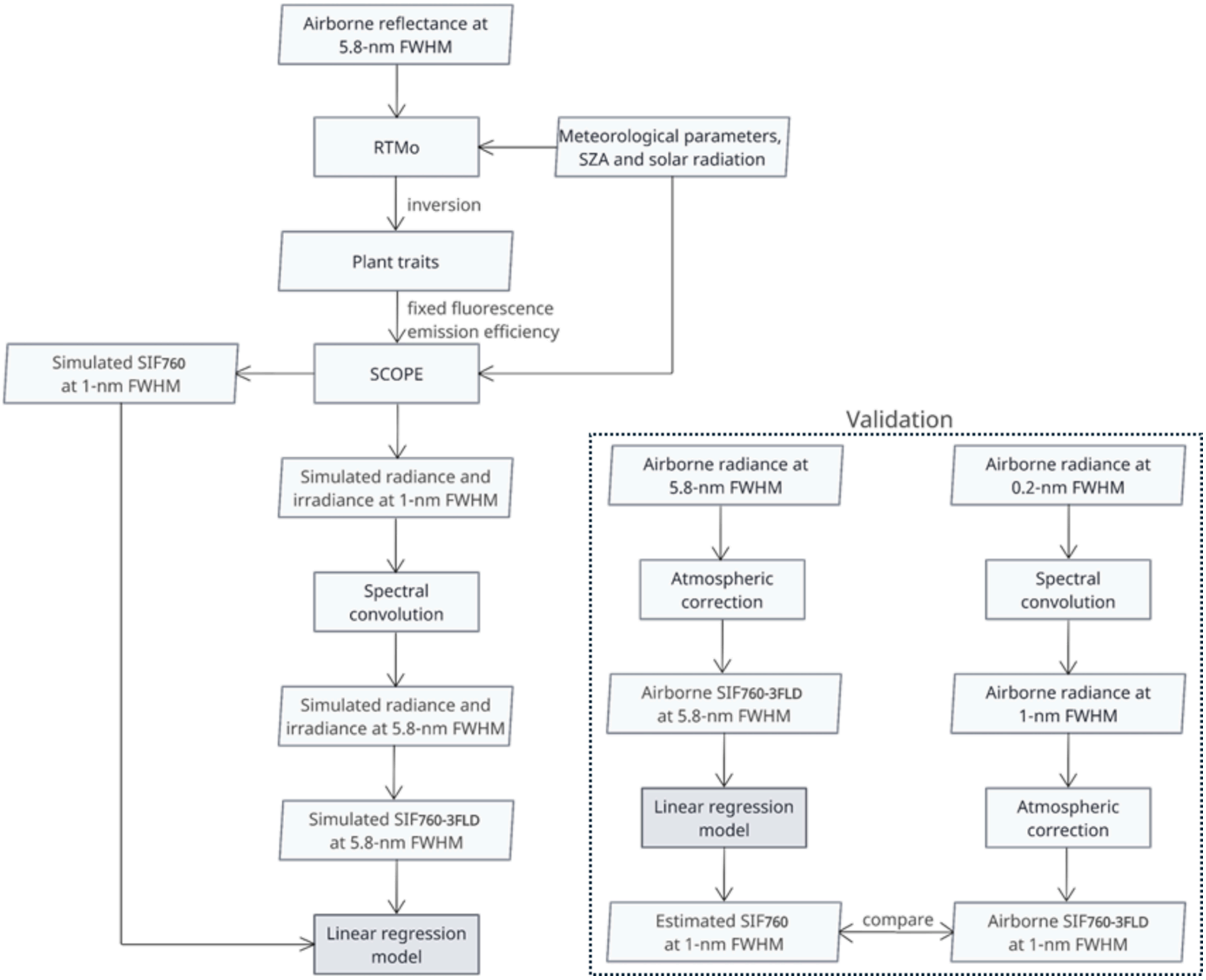

Fig. 3. Overview of the methodology used for estimating SIF_{760} at 1-nm FWHM from the narrow-band airborne hyperspectral imager.

Table 3
The ranges, standard deviations (sd), and initial values of free parameters used in numerical optimisation approach.

Parameter	Range		Initial value		Assumed sd		Unit
	Site 1	Site 2	Site 1	Site 2	Site 1	Site 2	
C_{a+b}	20–60	40–80	35	40	10	30	μg/cm^2
C_{dm}	0–20	0–20	10	1	20	20	mg/cm^2
C_w	0–20	0–20	1	10	6	6	mg/cm^2
C_s	0–0.4	0–0.4	0.1	0.001	0.2	0.2	–
C_{ca}	0–25	1–20	10	10	2	4	μg/cm^2
C_{ant}	0–8	0–8	0.1	5	12	12	μg/cm^2
N	1–3	0.5–2	1.5	1.5	0.75	0.75	–
1–exp (–0.2LAI)	0.1–0.7	0.1–0.8	0.45	0.55	0.6	0.2	m^2/m^2
$LIDF_a$ + $LIDF_b$	−1–1	−1–1	−0.35	−0.35	0.4	0.6	–
$LIDF_a$–$LIDF_b$	−1–1	−1–1	−0.2	−0.35	0.4	0.6	–

senescence parameters (C_s), leaf area index (LAI), leaf structure parameter (N) and leaf inclination distribution function parameters ($LIDF_a$ and $LIDF_b$). Average leaf angle (ALA) was calculated from the modelled $LIDF_a$ ($ALA = 45 - 360 \times LIDF_a \times \frac{1}{\pi^2}$) (Verhoef, 1998). Assuming the sensor view angle remains spatially constant for a single narrow-band imagery and in the nadir direction, the solar zenith angles were computed to be 54.8° for Site 1 and 26° for Site 2 based on the time and place of the imagery acquisition. Furthermore, based on MODTRAN simulations and the portable weather station data, the direct and diffused irradiance as well as meteorological parameters (air temperature and air pressure) specific to each study site were computed for executing the RTMo model. The 'lsqnonlin' function in MATLAB R2022b (MATLAB; Optimisation Toolbox; MathWorks Inc., Natick, MA, USA) was employed to update parameter values at each iteration step, and the iteration process concluded when the cost function improvement reached below a threshold of 10^{-4}. We conducted additional analysis to assess the reliability of the estimated plant traits. This analysis was performed on a nitrogen fertilisation validation block consisting of twenty plots with five distinct nitrogen treatments at Site 1 (T1: 0 kg N/ha, T2: 46 kg N/ha, T3: 92 kg N/ha, T4: 138 kg N/ha, T5: 184 kg N/ha). We evaluated the estimated C_{a+b} using the mean leaf-level measurements categorised by N fertiliser treatment (Fig. S1a in Supplementary data). In the absence of field measurements, the structural parameter LAI could only be compared to the related narrow band index, the Enhanced Vegetation Index (EVI). (Fig. S1b in Supplementary data).

The SCOPE model was run in forward mode using the estimated plant traits and the meteorological parameters (air temperature and air pressure) specific to each study site as inputs, as well as the MODTRAN simulated diffused and direct solar radiation. All inputs, except for ϵ_F were set to their default values according to SCOPE. The value of ϵ_F was modified to 0.014, representing a 40 % increase compared to the default value of 0.01 for dark-adapted leaf. This adjustment was made based on the premise that this value accurately reflects the steady-state fluorescence during daylight hours (Van der Tol et al., 2014). As with other simulations, the default 1-nm SR outputs were convolved to match the spectral resolution of the narrow-band hyperspectral imager using Gaussian spectral response function. The convolved 5.8-nm FWHM resolution SCOPE simulated radiance spectra were compared to the narrow-band imager derived airborne radiance. Furthermore, the depth of O_2-A absorption feature and near-infrared reflectance of vegetation (NIRv) (Badgley et al., 2017) were quantified from the simulated and airborne spectra. Such comparison enables the assessment of the consistency between simulated and airborne spectra. We calculated the depth of the O_2-A absorption feature based on the radiance difference between the left shoulder wavelength and the wavelength at the bottom of the absorption feature (Belwalkar et al., 2022). The wavelength within the 750–755 nm range that exhibited the highest radiance was identified as the left shoulder wavelength.

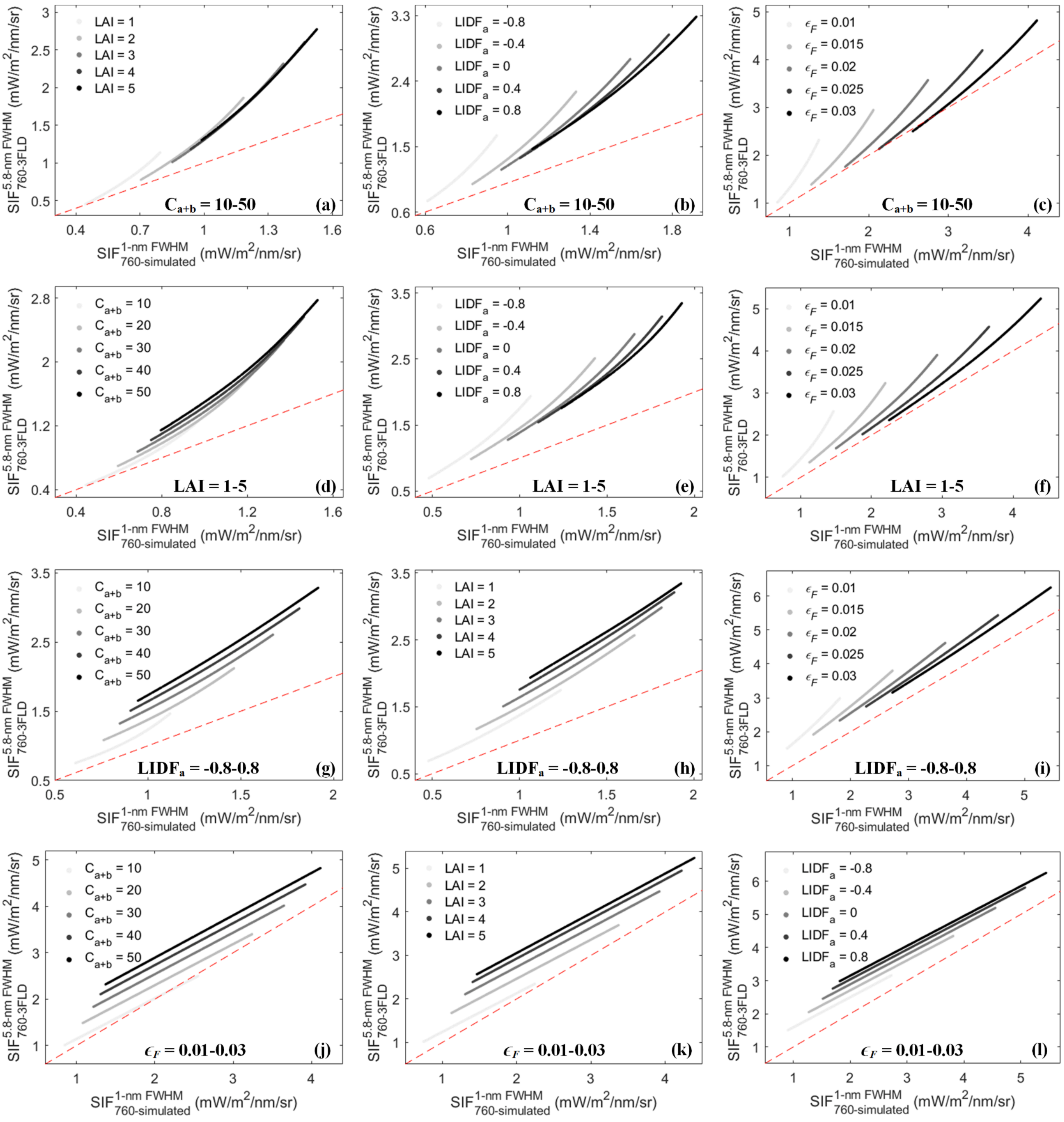

Fig. 4. Effects of ϵ_F and leaf biochemical and structural traits on the relationship between $SIF_{760\text{-}3FLD}$ quantified at 5.8-nm FWHM and $SIF_{760\text{-simulated}}$ at 1-nm FWHM directly simulated by SCOPE. Traits include C_{a+b} (a-c), LAI (d-f), $LIDF_a$ (g-i), and ϵ_F (j-l). Five distinct values corresponding to one of the remaining three parameters were assigned for each varying parameter (for example C_{a+b} in a-c), thereby producing a family of curves. All other SCOPE input parameters were left at their default settings. The dashed red line depicts the 1:1 line.

Using the convolved 5.8-nm FWHM simulated radiance and simulated irradiance spectra corresponding to both study sites, $SIF_{760\text{-}3FLD}$ was computed following the same methodology as outlined in section 2.2. We evaluated a linear regression model for estimating 1-nm SR SIF_{760} from the 5.8-nm FWHM narrow-band spectra. The linear model corresponding to each site was developed by using convolved 5.8-nm SR $SIF_{760\text{-}3FLD}$ as the independent variable and 1-nm SR $SIF_{760\text{-simulated}}$ as the dependent variable. The linear model independently developed for each study site using the simulated 5.8-nm SR $SIF_{760\text{-}3FLD}$ and 1-nm SR $SIF_{760\text{-simulated}}$ datasets was subsequently utilised to estimate airborne SIF_{760} at 1-nm FWHM from narrow-band imager quantified $SIF_{760\text{-}3FLD}$. The performance evaluation of the linear regression models for both sites was conducted using sub-nanometer-resolution airborne hyperspectral imagery acquired concurrently with narrow-band resolution imagery. The sub-nanometer resolution radiance spectra corresponding to the selected validation plots (as in Belwalkar et al., 2022) were convolved to the default SCOPE spectral characteristics to compute 1-nm SR $SIF_{760\text{-}3FLD}$, which served as a reference to validate the estimated 1-nm SR SIF_{760} from the 5.8-nm FWHM resolution narrow-band hyperspectral imager. The computation of 1-nm SR $SIF_{760\text{-}3FLD}$ from the convolved sub-nanometer-resolution airborne spectra was carried out following the same procedure as outlined in Section 2.2 for quantifying $SIF_{760\text{-}3FLD}$ from the narrow-band hyperspectral imager. Plot-level 1-nm SR SIF_{760} estimated from linear regression models was compared to the sub-nanometer derived reference $SIF_{760\text{-}3FLD}$ using coefficient of determination (R^2), root mean square error (RMSE), and normalised root mean square error (nRMSE) as evaluation metrics. The nRMSE was computed as the ratio of RMSE and mean of reference $SIF_{760\text{-}3FLD}$.

3. Results

The sensitivity of the relationship between SCOPE-derived $SIF_{760\text{-}3FLD}$ at 5.8-nm FWHM and $SIF_{760\text{-simulated}}$ at 1-nm FWHM to ϵ_F and leaf biochemical and structural traits is presented in Fig. 4. Overall, $SIF_{760\text{-}3FLD}$ increased with increasing values of C_{a+b}, LAI, $LIDF_a$, and ϵ_F for all scenarios; however, the relationship between SIF at 1- and 5.8-nm SRs varied widely across simulations. Narrow-band $SIF_{760\text{-}3FLD}$ tended to be overestimated as plant trait parameters increased, with a non-linear response to changing C_{a+b} (Fig. 4a–c) and LAI (Fig. 4d–f), but a linear response to varying $LIDF_a$ (Fig. 4g–i) and ϵ_F (Fig. 4j–l).

Fig. 5 shows the comparison of the modelled reflectance obtained via NO approach and the narrow-band imager derived measured reflectance for the two study sites, along with the residuals (the measured minus simulated spectra). In general, NO approach accurately reproduced the reflectance with RMSE in the range of 0.0049–0.01. Nevertheless, there were noticeable differences between the modelled spectra and those derived from the narrow-band images. In particular, the modelled reflectance peak at the wavelength of 550 nm in the green spectral region exhibited excessive sharpness, particularly in relation to Site 2 (Fig. 5b). This phenomenon can be attributed to the absorption spectra of carotenoids and chlorophyll, which are utilised as input in the Fluspect model (Van der Tol et al., 2016).

The ranges of values for the three important plant traits (C_{a+b}, LAI, and ALA) estimated via NO approach for the validation plots are shown in Fig. 6. The substantial differences in estimated plant traits between the two study sites can be attributed to differences in crop type, irrigation regime, and meteorological conditions. All three estimated plant traits were more variable at Site 1 than at Site 2, as expected, given the use of multiple cultivars and a wider range of nitrogen treatments. Using the NO approach, the estimated C_{a+b} for the N treatment validation block at Site 1 showed good agreement with leaf-level C_{a+b} measurements ($R^2 = 0.71$; RMSE $= 1.25$ μg/cm^2, Fig. S1a in Supplementary data). It also precisely captured the trends observed in the leaf-level measurements for different N treatments, indicating the reliability of the NO approach. Furthermore, the estimated LAI exhibited a strong significant relationship ($R^2 = 0.97$; $p < 0.001$, Fig. S1b in Supplementary data) with EVI, indicating that the NO approach effectively retrieved the structural plant traits. The resulting plot-scale spatial variability associated with the estimated C_{a+b} and LAI within the entire experimental field at Site 1 is depicted in Fig. 7.

The convolved TOC radiance spectra at 5.8-nm FWHM simulated using SCOPE forward modelling and the measured airborne at-sensor radiance from the narrow-band imager for Site 1 within the 400- to 800-nm region matched reasonably well (Fig. 8a–d). The depth of O_2-A absorption band and NIRv quantified from the simulated and the measured airborne spectra yielded strong significant relationships ($R^2 =$ 0.95–0.99; Fig. 8e and f). For Site 2, similar agreement was found among the at-sensor radiance spectra obtained from the two airborne hyperspectral imagers and the convolved TOC radiance spectra at 5.8-nm FWHM simulated using SCOPE forward modelling within the 670–780 nm region (Fig. 9). For both sites, discrepancies were observed for the simulated TOC radiance within the O_2-A absorption region. Specifically, a consistent underestimation of the O_2-A band depth corresponding to the simulated radiance was observed when compared to the O_2-A band depth derived from airborne at-sensor radiance. This outcome is anticipated as the O_2-A band depth increases with sensor altitude (Daumard et al., 2015; Ni et al., 2016).

The results of the forward SCOPE model simulations using the estimated plant traits as inputs revealed a substantial linear relationship between 1-nm SIF_{760} and 5.8-nm $SIF_{760\text{-}3FLD}$ for the simulated datasets ($R^2 = 0.99$; nRMSE $= 45.5$ %; slope $= 0.541$; offset $= 0.026$ for Site 1 and $R^2 = 0.92$; nRMSE $= 52.1$ %; slope $= 0.427$; offset $= 0.455$ for Site 2, respectively). The slope and offset of this linear relationship between simulated SIF datasets corresponding to both study sites were subsequently applied to the 5.8-nm FWHM airborne narrow-band $SIF_{760\text{-}3FLD}$ to estimate airborne SIF_{760} at 1-nm FWHM (Fig. 10). $SIF_{760\text{-}3FLD}$ quantified from the narrow-band imager were overestimated compared to the

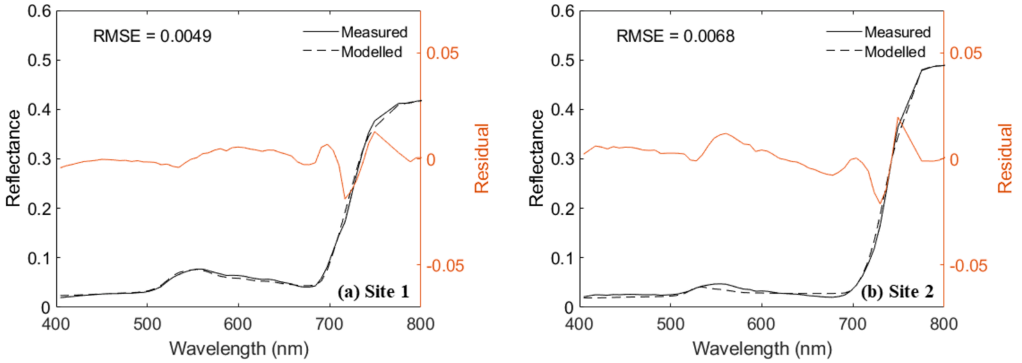

Fig. 5. Comparison of spectra obtained from SCOPE model inversion and image average spectra for Site 1 (a) and Site 2 (b). The right y-axis shows the residual which is computed as the difference between measured and modelled reflectance.

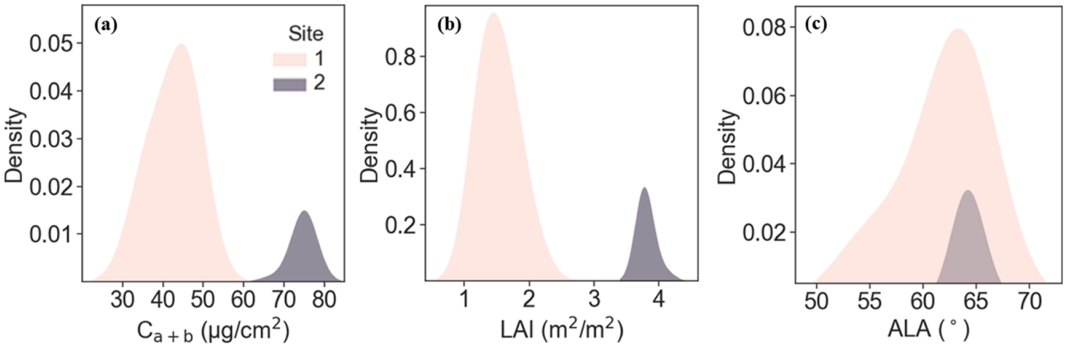

Fig. 6. Ranges of variation for the leaf biochemical and structural traits estimated from the narrow-band hyperspectral imagery at the two study sites: C_{a+b} (a), LAI (b), and ALA (c).

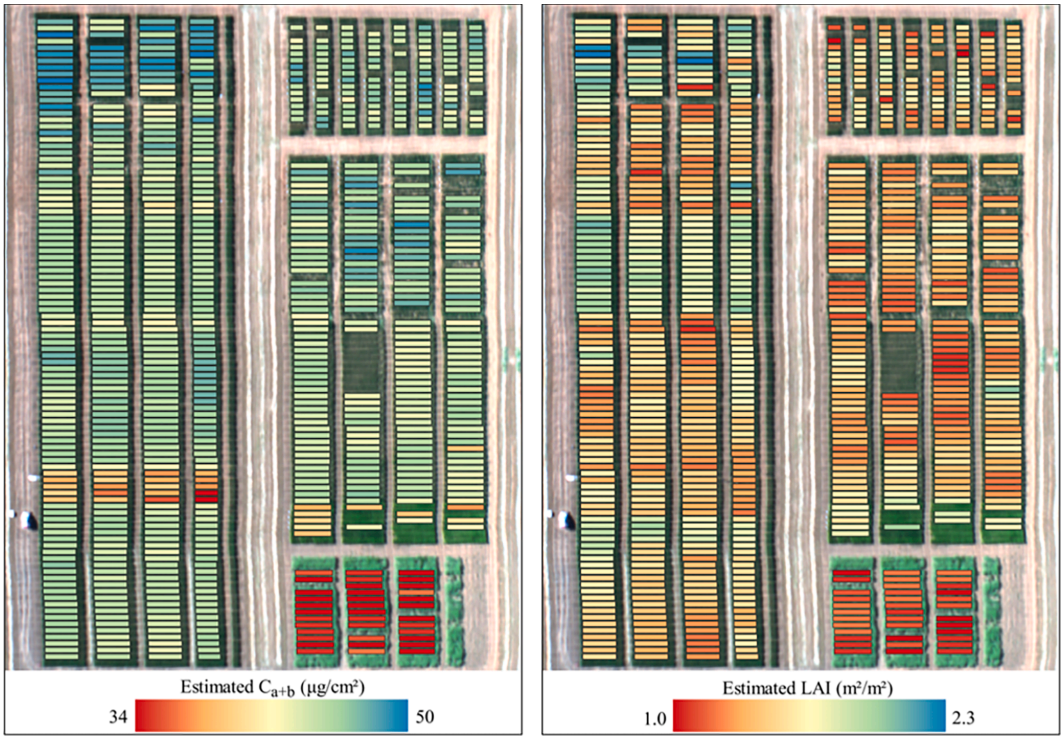

Fig. 7. Maps of estimated C_{a+b} (μg/cm^2) (a) and LAI (m^2/m^2) (b) at plot scale depicting the within-field variability at Site 1.

1-nm SR reference (RMSE = 2.23 mW/m^2/nm/sr for Site 1 and RMSE = 2.12 mW/m^2/nm/sr for Site 2) due to the spectral characteristics of the narrow-band imager. Nevertheless, narrow-band $SIF_{760\text{-}3FLD}$ were significantly correlated with the high-SR reference at both Site 1 ($R^2 = 0.93, p < 0.001$; Fig. 10a) and Site 2 ($R^2 = 0.95, p < 0.001$; Fig. 10b). The RMSEs for narrow-band SIF_{760} estimates scaled with the linear model were less than 0.5 mW/m^2/nm/sr. The linear model overestimated 1-nm SR SIF_{760} at Site 1 (nRMSE = 24.9 %; Fig. 10c) and slightly underestimated it at Site 2 (nRMSE = 7.77 %; Fig. 10d). A plot-scale visualisation of scaled linear model estimates from the narrow-band hyperspectral imager for the entire field at Site 1 is shown in Fig. 11.

4. Discussion

In precision agriculture, plant phenotyping studies, and other high-throughput applications, the complexity and operational costs of sub-nanometer airborne imaging sensors make alternative sensors appealing, if SIF can be measured accurately. Previous theoretical work using the SCOPE model has evaluated the most critical parameters affecting SIF via global sensitivity analysis (Verrelst et al., 2015). Our study builds on this theoretical work by considering how narrow-band sensors affect SIF retrieval and by validating theoretical quantifications against high-resolution experimental field data. Extending recent work by Belwalkar et al. (2022), we evaluated a novel modelling methodology to accurately quantify SIF_{760} at 1-nm FWHM from standard narrow-band-resolution imaging sensors using SCOPE RTM.

The impact of SR on SIF was theoretically assessed using the SCOPE model, with ϵ_F and leaf biochemical and structural traits being independently varied. The results illustrated a trait-dependent link between the 1-nm FWHM $SIF_{760\text{-}simulated}$ and 5.8-nm FWHM $SIF_{760\text{-}3FLD}$. Non-linear variations were observed in relation to C_{a+b} and LAI, while linear variations were observed in relation to $LIDF_a$ and ϵ_F (Fig. 4). The results suggest that coarser resolution SIF_{760} levels can be scaled to 1-nm FWHM by considering the impact of ϵ_F and leaf biochemical and structural traits on the interrelationship between SIF_{760} at different SR using a suitable mapping function. The selection of this mapping function is dependent on the traits being varied. By simultaneously varying the four parameters drawn from a uniform distribution within the same

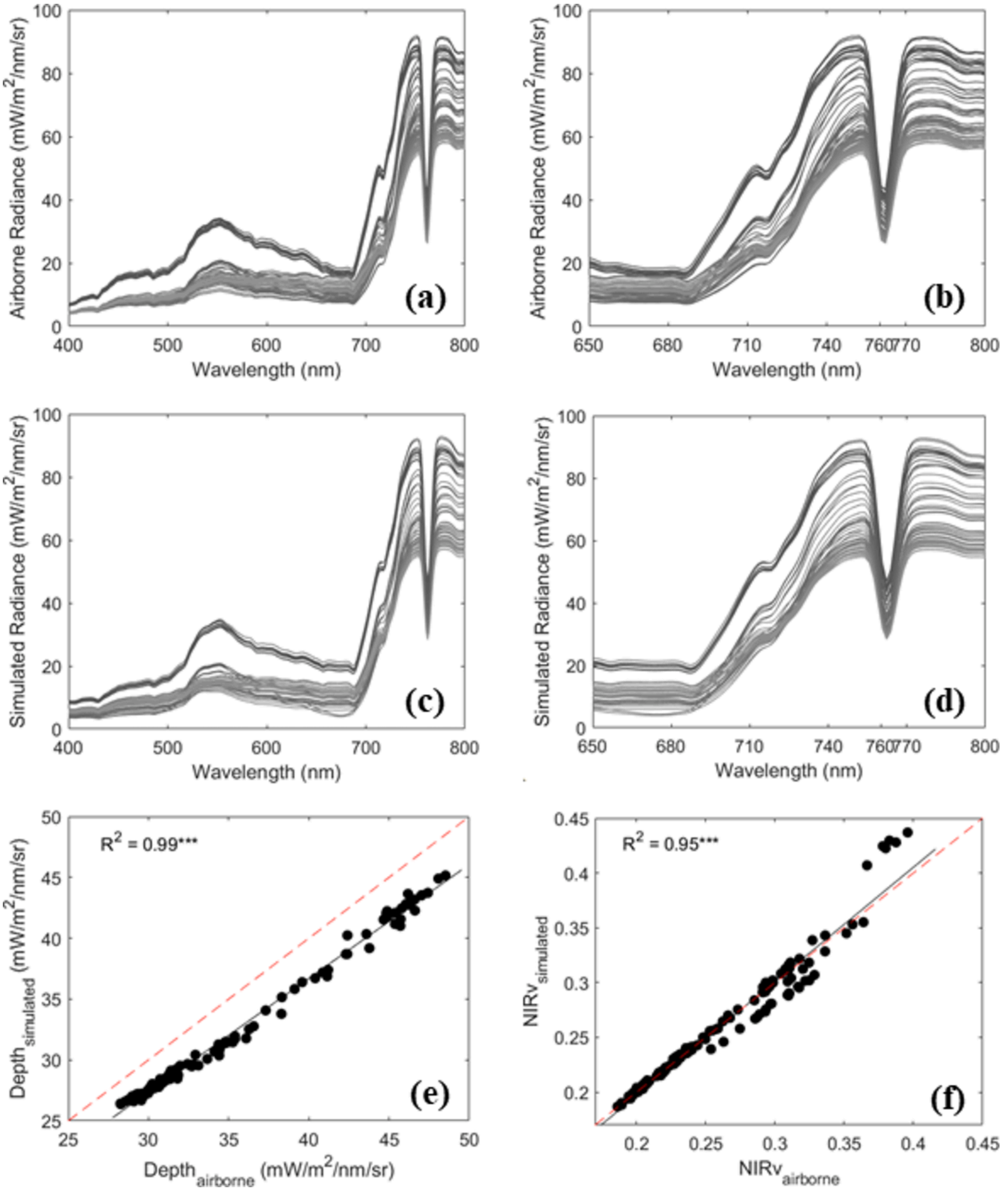

Fig. 8. Comparison of radiance spectra obtained from the narrow-band imager (a, b) and simulated spectra (c, d) obtained from SCOPE forward mode simulation (using the estimated plant traits) for Site 1 in the 400- to 800-nm region, and in the SIF emission region, respectively. Relationship between depth at the O_2-A absorption feature (e) and NIRv (f) quantified from the simulated and airborne spectra for Site 1. The simulated spectra were obtained after convolving the original 1-nm FWHM SCOPE spectra to the spectral characteristics of the narrow-band imager using Gaussian convolution. ****p*-value <0.001.

ranges as in Fig. 4, we found a strong linear relationship ($R^2 = 0.93$; RMSE = 0.62 mW/m^2/nm/sr) between the 1-nm FWHM $SIF_{760\text{-simulated}}$ and 5.8-nm FWHM $SIF_{760\text{-3FLD}}$ (Fig. S2 in Supplementary data). This result further demonstrates the feasibility of scaling coarser resolution SIF_{760} to a finer resolution for a diverse range of most significant plant traits impacting SIF.

Leaf biochemical and structural traits, as well as sun-target geometry, are the primary drivers of TOC SIF and reflectance, which undergo comparable radiative transfer processes within leaves and canopies (Yang et al., 2019). As a result, the biochemical and biophysical impacts of vegetation on canopy SIF can be characterised by combining RTM with canopy reflectance (Van der Tol et al., 2019; Yang and van der Tol, 2018). Prior studies (Van der Tol et al., 2016; Wang et al. 2023; Yang et al., 2019) have demonstrated that the parameters estimated from reflectance can replicate a large portion of the SIF variability, and the uncertainty in simulated SIF is impacted by the accuracy of the reflectance fitting. In our study, the modelled reflectance closely aligned with the airborne reflectance at both study sites, with RMSE ranging from 0.0049 to 0.01 (Fig. 5), consistent with Wang et al. (2023) and Yang et al. (2019). The low RMSE between the modelled and measured airborne reflectance demonstrates the reliability of the inverted traits and the robustness of the inversion methodology. In addition, the validation of estimated C_{a+b} using the leaf-level readings (Fig. S1a in Supplementary data) and the estimated LAI using EVI (Fig. S1b in Supplementary data) indicated that the inversion methodology well captured the observed leaf-level trends associated with different N treatments, thereby confirming the accuracy of the estimated plant traits. Furthermore, to reduce the ill-posedness of the inversion, we restricted the ranges of certain parameters based on the variations in meteorological conditions, crop type, and irrigation regime between the

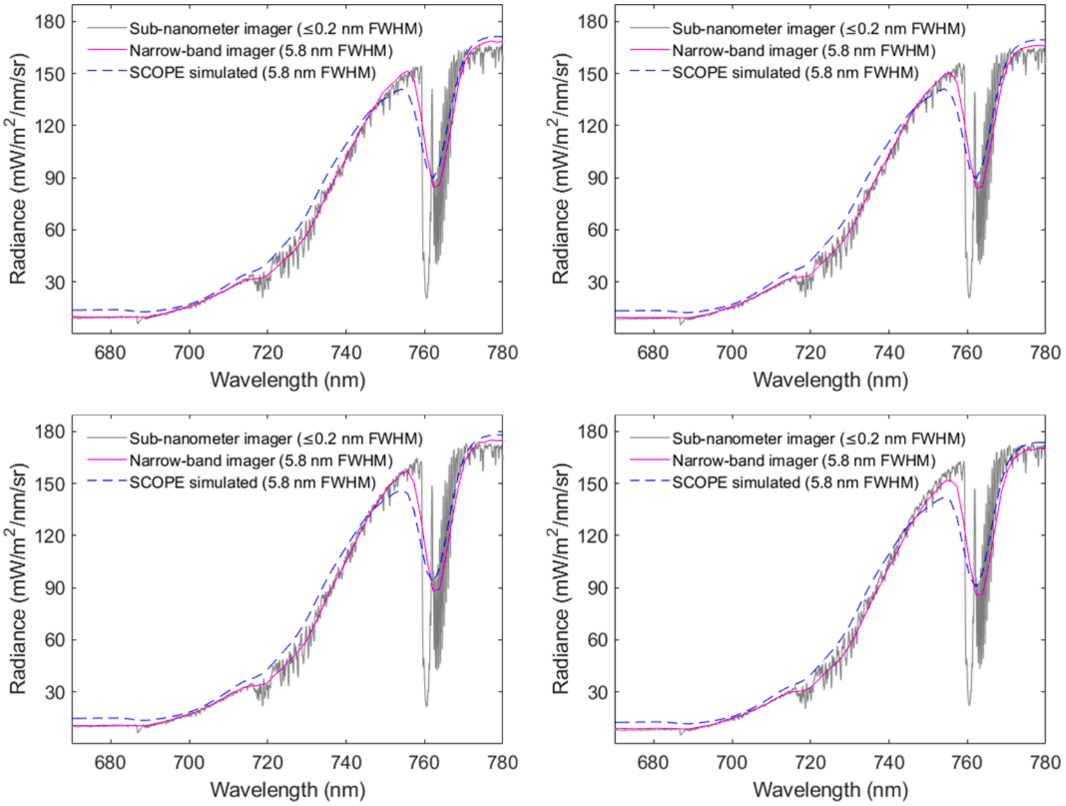

Fig. 9. Comparison of radiance spectra obtained from the two airborne hyperspectral imagers and simulated spectra obtained from SCOPE forward mode simulation (using the estimated plant traits) for Site 2.

two study sites. For instance, C_{a+b} was confined to 20–60 μg/cm^2 for Site 1 and 40–80 μg/cm^2 for Site 2 (Table 3).

Our results revealed that the SIF_{760} quantified from broader SR hyperspectral imager (5.8-nm FWHM) using the proposed modelling approach aligned well ($R^2 = 0.93$–0.95; RMSE = 0.203–0.425 mW/m^2/nm/sr; Fig. 10) with $SIF_{760\text{-}3FLD}$ quantified at 1–nm FWHM from the sub-nanometer airborne imager flown in tandem and used for validation across two plant phenotyping experimental sites showing nutrient stress variability. Our findings support the operational viability of using standard, commercially accessible, low-cost narrow-band hyperspectral imaging sensors to obtain accurate absolute SIF_{760} levels in phenotyping trials of homogeneous and uniform canopies.

TOC SIF is affected by various factors including plant pigments, canopy structure, incident solar radiation, meteorological conditions, and sensor spectral configuration. The RTM-based methodology proposed in this study facilitates the comprehensive evaluation of all these factors for the accurate SIF quantification. Considering that the aforementioned factors affecting SIF vary by location, it is very challenging to develop a generalised model applicable to all sites. Furthermore, the requirement for precise parameterisation to estimate plant traits unique to each site makes the proposed modelling approach inherently site-specific. Nevertheless, the overall methodology is relatively straightforward to apply to other sites with homogeneous crop canopies. The study demonstrates the relationship between sub-nanometer and broader band SIF_{760}, offering insights and methods that are applicable across a diverse range of study sites.

It is possible to obtain an approximation of ϵ_F from narrow-band imagery using SIF_{760} and NIRv-based approaches (Dechant et al., 2020; Zeng et al., 2022). However, the higher SIF_{760} levels quantified from narrow-band imaging sensors would invariably result in over-estimation of ϵ_F estimates. It is not feasible to estimate accurate ϵ_F directly from narrow-band imagery, as the SCOPE model necessitates an accurate value of ϵ_F for precise SIF modelling. Therefore, we opted to keep ϵ_F constant in the absence of leaf-level fluorescence parameters that could be used to precisely determine ϵ_F. Nevertheless, narrow-band derived ϵ_F estimates can still be used to examine the relative physiological variability within the field, particularly for stress detection studies. Future studies will involve the measurement of fluorescence parameters at the leaf level to determine accurate ϵ_F, which can be utilised to generate a more accurate SIF_{760} from narrow-band imaging sensor.

TOC SIF simulations were carried out by utilising plant traits derived from airborne narrow-band reflectance imagery, while keeping the ϵ_F constant. Hence, the observed variability in simulated SIF among the plots at both study sites may be solely attributed to differences in the absorption of photosynthetically active radiation (PAR) and the re-absorption of SIF, while being unaffected by the efficiency of fluorescence emission. Consequently, the dissimilarities seen between the reference $SIF_{760\text{-}3FLD}$ at 1-nm and the estimated SIF_{760} at 1-nm using the linear model for the airborne datasets may potentially be attributed to variances in plant physiology, which are incorporated into the model via the parameter ϵ_F. For Site 1, the estimated SIF_{760} values were over-estimated which suggests that the actual ϵ_F of the plots deviated from the predetermined value of 0.014, assuming that the estimated plant traits were accurate. In contrast, Site 2 exhibited a better correspondence between the calculated SIF_{760} and the reference $SIF_{760\text{-}3FLD}$, indicating that the parameter ϵ_F for all the plots was close to 0.014.

The effect of sensor noise on the SIF_{760} scaling methodology proposed in this study is important to consider in an operational context, as SIF is strongly influenced by sensor SNR. Because the linear model was trained on noise-free simulated SCOPE spectra in this study, this method is not recommended for pixel-based analysis using sensors with low SNR levels. Instead, analyses should be limited to an object-based scale in which pixels are averaged across individual areas to minimise the impact of SNR. Future research could characterise the effect of sensor noise through the addition of noise to the simulated dataset, thereby

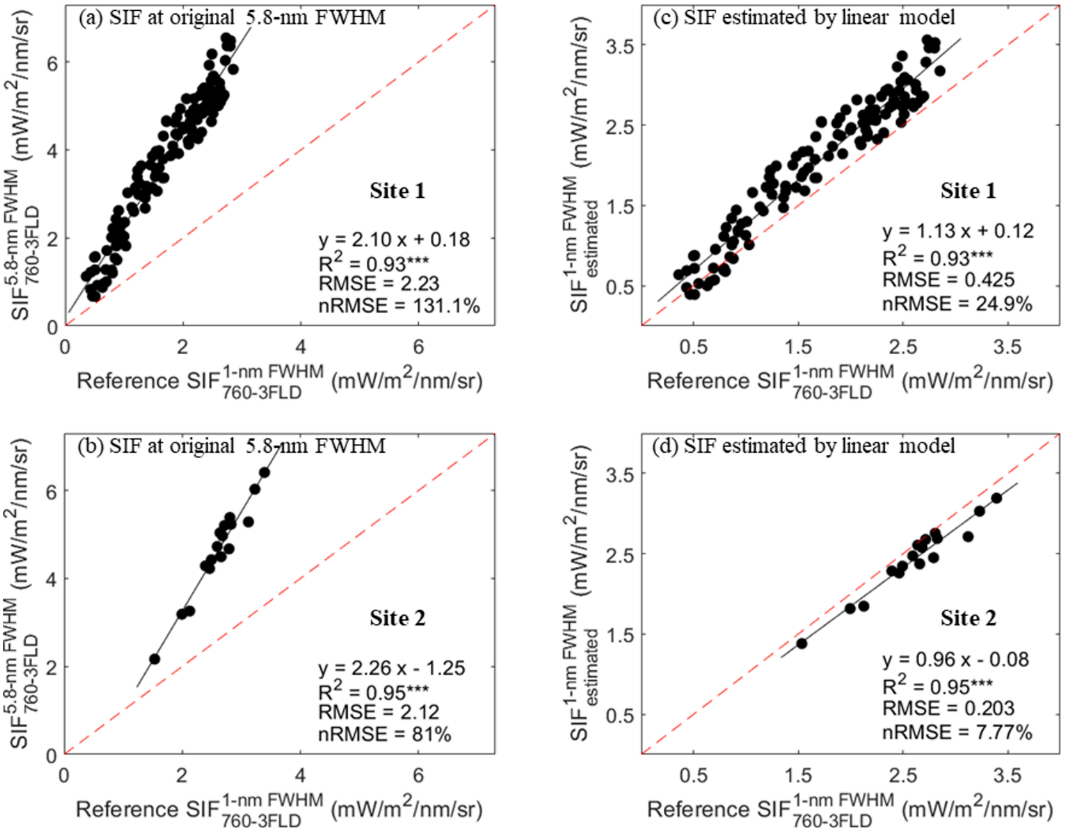

Fig. 10. Relationships between the airborne $SIF_{760\text{-}3FLD}$ quantified from the sub-nanometer imager (used here as the reference SIF) and narrow-band imager (5.8-nm FWHM) for validation plots corresponding to both sites (a, b). Relationships between the airborne $SIF_{760\text{-}3FLD}$ quantified from the sub-nanometer imager and the airborne 1-nm SR SIF_{760} estimated by the linear model (c, d) from the 5.8-nm SR narrow-band airborne spectra for both sites. The reference 1-nm SR $SIF_{760\text{-}3FLD}$ was obtained by convolving the sub-nanometer resolution spectra to 1-nm FWHM. The red dashed and black solid lines depict the 1:1 line and regression line, respectively. $^{***}p$-value <0.001.

enabling the quantification of SIF_{760} at the pixel scale and the generation of SIF_{760} pixel-level maps from standard narrow-band imaging sensors with low SNR. In the current study, the SIF_{760} scaling approach was designed and validated for phenotyping experiments involving nutrient variability as part of nitrogen application treatments, causing nutrient deficiency and stress. Future research will focus on evaluating the proposed scaling approach for canopies subjected to other abiotic stresses, such as under water limiting conditions, and under biotic-induced stress (see Zarco-Tejada et al. (2021) for the significance of SIF for separating biotic from abiotic stress). Such research will be critical for understanding the potential of standard narrow-band imaging sensors for obtaining accurate SIF_{760} across a wide range of ecosystems.

Although a recent version of the SCOPE model (version 2.0) accounts for the vertical heterogeneity of the canopy biophysical and biochemical properties, it retains the assumption of homogeneity in the horizontal direction (Yang et al., 2021). Thus, our methods based on SCOPE parametrisation are most applicable in experimental fields with homogeneous crop canopies. It will also be important to further investigate the scaling approach described in this paper over complex and heterogeneous canopies, such as forests, and row-structured and grid-based crop canopies such as vineyards and tree orchards. Such efforts will require the extraction of crown spectra from pure vegetation pixels from very-high-spatial-resolution hyperspectral imagery to minimise the impact of the structural heterogeneity. Alternatively, three-dimensional canopy RTMs capable of directly simulating canopies with tree crowns, such as FluorFLIGHT (Hernández-Clemente et al., 2017), the Fluorescence model with Weight Photon Spread (FluorWPS) (Zhao et al., 2016), and the Discrete Anisotropic Radiative Transfer (DART) model (Gastellu-Etchegorry et al., 2017), could be employed. Such studies would be relevant for future missions such as the FLuorescence EXplorer (FLEX) (Drusch et al., 2017) when attempting to monitor the fluorescence emission in forests and heterogeneous crops.

5. Conclusions

We proposed a modelling scheme based on SCOPE for spectrally scaling $SIF_{760\text{-}3FLD}$ quantified from a standard airborne hyperspectral imager of 5.8-nm FWHM to SIF at 1-nm FWHM. Validation was carried out using $SIF_{760\text{-}3FLD}$ quantified from sub-nanometer hyperspectral imagery acquired from two experimental fields with different homogenous crop canopies. There was strong agreement between estimated and reference SIF_{760}, yielding RMSEs lower than 0.5 mW/m^2/nm/sr and R^2 of 0.93–0.95. Our findings show that scaling $SIF_{760\text{-}3FLD}$ retrievals with standard 4–6 nm FWHM hyperspectral imagery to finer spectral resolutions using RTM-based modelling methods is feasible and address the problem of the $SIF_{760\text{-}3FLD}$ overestimation when using hyperspectral imagers with FWHM $>$ 1-nm and SSI $\geq$ 1-nm.

In summary, the need for an accurate quantification of SIF is critical from an operational perspective, particularly because sub-nanometer hyperspectral imagers are not readily available in agronomic settings and for practical purposes. Consequently, it is essential to consider the adoption of suitable airborne imaging sensors, as well as the development of methods based on physically-based models for correctly interpreting SIF from standard sensors, particularly in cases where they have coarser spectral resolutions (greater than 1-nm FWHM). The selection of appropriate physically-based models based on the type of ecosystem under consideration, especially for complex heterogeneous canopies, and the proper modelling approach are additional factors to consider.

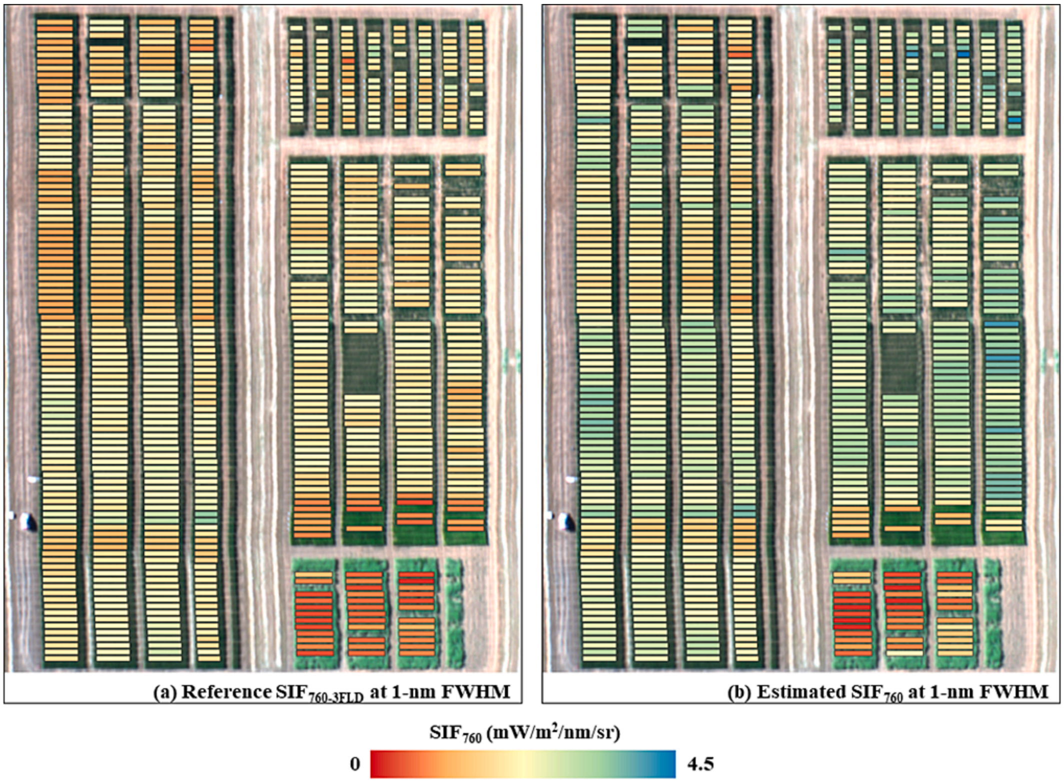

Fig. 11. Plot-scale maps of reference SIF$_{760\text{-}3FLD}$ from sub-nanometer imager (a) and estimated SIF$_{760}$ from narrow-band imager (b) using the linear model at 1-nm FWHM for Site 1. The reference 1-nm SR SIF$_{760\text{-}3FLD}$ was obtained by convolving the sub-nanometer resolution spectra to 1-nm FWHM.

Accounting for the aforementioned considerations will facilitate the use of accurately quantified SIF from imaging sensors onboard piloted and unmanned airborne platforms for the advancement of research on photosynthesis, physiological assessment and pre-visual stress detection.

CRediT authorship contribution statement

A. Belwalkar: Writing – review & editing, Writing – original draft, Methodology, Investigation, Formal analysis, Conceptualization. **T. Poblete:** Writing – review & editing, Supervision, Methodology, Conceptualization. **A. Hornero:** Writing – review & editing. **R. Hernández-Clemente:** Writing – review & editing. **P.J. Zarco–Tejada:** Writing – review & editing, Supervision, Project administration, Methodology, Conceptualization.

Declaration of competing interest

The authors declare that they have no known competing financial interests or personal relationships that could have appeared to influence the work reported in this paper.

Data availability

The authors do not have permission to share data.

Acknowledgements

This research was supported by The University of Melbourne's Research Computing Services and the Petascale Campus Initiative. The authors gratefully acknowledge the Foundation for Arable Research Australia, in particular Michael Straight and Ben Morris; the Grains Research and Development Corporation Australia; and Riverine Plains Incorporated for their provision and management of the field trials. A. Longmire, A. Gracia–Romero and Y. Wang are acknowledged for their technical support during the field and airborne campaigns. We are also grateful for the constructive comments of N. Wang regarding numerical optimisation methodology.

Appendix A. Supplementary data

Supplementary data to this article can be found online at https://doi.org/10.1016/j.jag.2024.104198.

References

Aasen, H., Honkavaara, E., Lucieer, A., Zarco-Tejada, P.J., 2018. Quantitative remote sensing at ultra-high resolution with UAV spectroscopy: A review of sensor technology, measurement procedures, and data correction workflows. Remote Sens. 10, 1091.

Badgley, G., Field, C.B., Berry, J.A., 2017. Canopy near-infrared reflectance and terrestrial photosynthesis. Sci. Adv. 3, e1602244.

Belwalkar, A., Poblete, T., Longmire, A., Hornero, A., Hernández-Clemente, R., Zarco-Tejada, P.J., 2022. Evaluation of SIF retrievals from narrow-band and sub-nanometer airborne hyperspectral imagers flown in tandem: modelling and validation in the context of plant phenotyping. Remote Sens. Environ. 273, 112986.

Berk, A., Conforti, P., Kennett, R., Perkins, T., Hawes, F., Van Den Bosch, J., 2014. MODTRAN® 6: A major upgrade of the MODTRAN® radiative transfer code. In: Proc. SPIE 9088, Algorithms and Technologies for Multispectral, Hyperspectral, and Ultraspectral Imagery XX, 90880H, 13 June 2014.

Braghiere, R.K., Wang, Y., Doughty, R., Sousa, D., Magney, T., Widlowski, J.L., Longo, M., Bloom, A.A., Worden, J., Gentine, P., Frankenberg, C., 2021. Accounting for canopy structure improves hyperspectral radiative transfer and sun-induced chlorophyll fluorescence representations in a new generation earth system model. Remote Sens. Environ. 261, 11249.

Brown, S.W., Eppeldauer, G.P., Lykke, K.R., 2006. Facility for spectral irradiance and radiance responsivity calibrations using uniform sources. Appl. Opt. 45, 8218–8237.

Calderón, R., Navas-Cortés, J.A., Lucena, C., Zarco-Tejada, P.J., 2013. High-resolution airborne hyperspectral and thermal imagery for early detection of Verticillium wilt of olive using fluorescence, temperature and narrow-band spectral indices. Remote Sens. Environ. 139, 231–245.

Camino, C., Zarco-Tejada, P.J., Gonzalez-Dugo, V., 2018a. Effects of heterogeneity within tree crowns on airborne-quantified SIF and the CWSI as indicators of water stress in the context of precision agriculture. Remote Sens. 10, 604.

Camino, C., González-Dugo, V., Hernández, P., Sillero, J.C., Zarco-Tejada, P.J., 2018b. Improved nitrogen retrievals with airborne-derived fluorescence and plant traits quantified from VNIR-SWIR hyperspectral imagery in the context of precision agriculture. Int. J. Appl. Earth Obs. Geoinf. 70, 105–117.

Camino, C., Gonzalez-Dugo, V., Hernández, P., Zarco-Tejada, P.J., 2019. Radiative transfer Vcmax estimation from hyperspectral imagery and SIF retrievals to assess photosynthetic performance in rainfed and irrigated plant phenotyping trials. Remote Sens. Environ. 231, 111186.

Campbell, P.K.E., Middleton, E.M., Corp, L.A., Kim, M.S., 2008. Contribution of chlorophyll fluorescence to the apparent vegetation reflectance. Sci. Total Environ. 404, 433–439.

Celesti, M., van der Tol, C., Cogliati, S., Panigada, C., Yang, P., Pinto, F., Rascher, U., Miglietta, F., Colombo, R., Rossini, M., 2018. Exploring the physiological information of Sun-induced chlorophyll fluorescence through radiative transfer model inversion. Remote Sens. Environ. 215, 97–108.

Cendrero-Mateo, M.P., Wieneke, S., Damm, A., Alonso, L., Pinto, F., Moreno, J., Guanter, L., Celesti, M., Rossini, M., Sabater, N., Cogliati, S., Julitta, T., Rascher, U., Goulas, Y., Aasen, H., Pacheco-Labrador, J., Mac Arthur, A., 2019. Sun-induced chlorophyll fluorescence III: benchmarking retrieval methods and sensor characteristics for proximal sensing. Remote Sens. 11, 962.

Chang, C.Y., Zhou, R., Kira, O., Marri, S., Skovira, J., Gu, L., Sun, Y., 2020. An Unmanned Aerial System (UAS) for concurrent measurements of solar-induced chlorophyll fluorescence and hyperspectral reflectance toward improving crop monitoring. Agric. For. Meteorol. 294, 108145.

Cogliati, S., Rossini, M., Julitta, T., Meroni, M., Schickling, A., Burkart, A., Pinto, F., Rascher, U., Colombo, R., 2015. Continuous and long-term measurements of reflectance and sun-induced chlorophyll fluorescence by using novel automated field spectroscopy systems. Remote Sens. Environ. 164, 270–281.

Damm, A., Erler, A., Hillen, W., Meroni, M., Schaepman, M.E., Verhoef, W., Rascher, U., 2011. Modeling the impact of spectral sensor configurations on the FLD retrieval accuracy of sun-induced chlorophyll fluorescence. Remote Sens. Environ. 115, 1882–1892.

Damm, A., Guanter, L., Paul-Limoges, E., Van der Tol, C., Hueni, A., Buchmann, N., Eugster, W., Ammann, C., Schaepman, M.E., 2015. Far-red sun-induced chlorophyll fluorescence shows ecosystem-specific relationships to gross primary production: an assessment based on observational and modeling approaches. Remote Sens. Environ. 166, 91–105.

Damm, A., Cogliati, S., Colombo, R., Fritsche, L., Genangeli, A., Genesio, L., Hanus, J., Peressotti, A., Rademske, P., Rascher, U., Schuettemeyer, D., Siegmann, B., Sturm, J., Miglietta, F., 2022. Response times of remote sensing measured sun-induced chlorophyll fluorescence, surface temperature and vegetation indices to evolving soil water limitation in a crop canopy. Remote Sens. Environ. 273, 112957.

Daumard, F., Goulas, Y., Ounis, A., Pedrós, R., Moya, I., 2015. Measurement and correction of atmospheric effects at different altitudes for remote sensing of sun-induced fluorescence in oxygen absorption bands. IEEE Trans. Geosci. Remote Sens. 53, 5180–5196.

Dechant, B., Ryu, Y., Badgley, G., Zeng, Y., Berry, J.A., Zhang, Y., Goulas, Y., Li, Z., Zhang, Q., Kang, M., Li, J., Moya, I., 2020. Canopy structure explains the relationship between photosynthesis and sun-induced chlorophyll fluorescence in crops. Remote Sens. Environ. 241, 111733.

Drusch, M., Moreno, J., Del Bello, U., Franco, R., Goulas, Y., Huth, A., Kraft, S., Middleton, E.M., Miglietta, F., Mohammed, G., Nedbal, L., Rascher, U., Schüttemeyer, D., Verhoef, W., 2017. The FLuorescence EXplorer mission concept - ESA's Earth Explorer 8. IEEE Trans. Geosci. Remote Sens. 55, 1273–1284.

Frankenberg, C., Köhler, P., Magney, T.S., Geier, S., Lawson, P., Schwochert, M., McDuffie, J., Drewry, D.T., Pavlick, R., Kuhnert, A., 2018. The chlorophyll fluorescence imaging spectrometer (CFIS), mapping far red fluorescence from aircraft. Remote Sens. Environ. 217, 523–536.

Gastellu-Etchegorry, J.-P., Lauret, N., Yin, T., Landier, L., Kallel, A., Malenovský, Z., Al Bitar, A., Aval, J., Benhmida, S., Qi, J., Medjdoub, G., Guilleux, J., Chavanon, E., Cook, B., Morton, D., Chrysoulakis, N., Mitraka, Z., 2017. DART: recent advances in remote sensing data modeling with atmosphere, polarization, and chlorophyll fluorescence. IEEE J. Sel. Top. Appl. Earth Obs. Remote Sens. 10, 2640–2649.

Gonzalez-Dugo, V., Hernández, P., Solis, I., Zarco-Tejada, P.J., 2015. Using high-resolution hyperspectral and thermal airborne imagery to assess physiological condition in the context of wheat phenotyping. Remote Sens. 7, 13586–13605.

Hao, D., Zeng, Y., Qiu, H., Biriukova, K., Celesti, M., Migliavacca, M., Rossini, M., Asrar, G.R., Chen, M., 2021. Practical approaches for normalizing directional solar-induced fluorescence to a standard viewing geometry. Remote Sens. Environ. 255, 112171.

Hao, D., Zeng, Y., Zhang, Z., Zhang, Y., Qiu, H., Biriukova, K., Celesti, M., Rossini, M., Zhu, P., Asrar, G.R., Chen, M., 2022. Adjusting solar-induced fluorescence to nadir-viewing provides a better proxy for GPP. ISPRS J. Photogramm. Remote Sens. 186, 157–169.

Hernández-Clemente, R., North, P.R.J., Hornero, A., Zarco-Tejada, P.J., 2017. Assessing the effects of forest health on sun-induced chlorophyll fluorescence using the FluorFLIGHT 3-D radiative transfer model to account for forest structure. Remote Sens. Environ. 193, 165–179.

Hornero, A., Zarco-Tejada, P.J., Quero, J.L., North, P.R.J., Ruiz-Gómez, F.J., Sánchez-Cuesta, R., Hernández-Clemente, R., 2021. Modelling hyperspectral- and thermal-based plant traits for the early detection of Phytophthora-induced symptoms in oak decline. Remote Sens. Environ. 263, 112570.

Julitta, T., Corp, L.A., Rossini, M., Burkart, A., Cogliati, S., Davies, N., Hom, M., Arthur, A.M., Middleton, E.M., Rascher, U., Schickling, A., Colombo, R., 2016. Comparison of sun-induced chlorophyll fluorescence estimates obtained from four portable field spectroradiometers. Remote Sens. 8, 122.

Köhler, P., Frankenberg, C., Magney, T.S., Guanter, L., Joiner, J., Landgraf, J., 2018. Global retrievals of solar-induced chlorophyll fluorescence with TROPOMI: first results and intersensor comparison to OCO-2. Geophys. Res. Lett. 45, 10, 456–10, 463.

Li, Z., Zhang, Q., Li, J., Yang, X., Wu, Y., Zhang, Z., Wang, S., Wang, H., Zhang, Y., 2020. Solar-induced chlorophyll fluorescence and its link to canopy photosynthesis in maize from continuous ground measurements. Remote Sens. Environ. 236, 111420.

Lichtenthaler, H.K., Rinderle, U., 1988. The role of chlorophyll fluorescence in the detection of stress conditions in plants. Crit. Rev. Anal. Chem. 19 (Suppl. 1), S29–S85.

Liu, X., Guanter, L., Liu, L., Damm, A., Malenovský, Z., Rascher, U., Peng, D., Du, S., Gastellu-Etchegorry, J.-P., 2019. Downscaling of solar-induced chlorophyll fluorescence from canopy level to photosystem level using a random forest model. Remote Sens. Environ. 231, 110772.

Liu, L., Liu, X., Hu, J., 2015. Effects of spectral resolution and SNR on the vegetation solar-induced fluorescence retrieval using FLD-based methods at canopy level. Eur. J. Remote Sens. 48, 743–762.

Longmire, A.R., Poblete, T., Hunt, J.R., Chen, D., Zarco-Tejada, P.J., 2022. Assessment of crop traits retrieved from airborne hyperspectral and thermal remote sensing imagery to predict wheat grain protein content. ISPRS J. Photogramm. Remote Sens. 193, 284–298.

Maimaitiyiming, M., Sagan, V., Sidike, P., Maimaitijiang, M., Miller, A.J., Kwasniewski, M., 2020. Leveraging very-high spatial resolution hyperspectral and thermal UAV imageries for characterizing diurnal indicators of grapevine physiology. Remote Sens. 12, 3216.

Meroni, M., Rossini, M., Guanter, L., Alonso, L., Rascher, U., Colombo, R., Moreno, J., 2009. Remote sensing of solar-induced chlorophyll fluorescence: review of methods and applications. Remote Sens. Environ. 113, 2037–2051.

Mohammed, G.H., Colombo, R., Middleton, E.M., Rascher, U., Van der Tol, C., Nedbal, L., Goulas, Y., Pėrez-Priego, O., Damm, A., Meroni, M., Joiner, J., Cogliati, S., Verhoef, W., Malenovský, Z., Gastellu-Etchegorry, J.P., Miller, J.R., Guanter, L., Moreno, J., Moya, I., Berry, J.A., Frankenberg, C., Zarco-Tejada, P.J., 2019. Remote sensing of solar-induced chlorophyll fluorescence (SIF) in vegetation: 50 years of progress. Remote Sens. Environ. 231, 111177.

Ni, Z., Liu, Z., Li, Z.L., Nerry, F., Huo, H., Sun, R., Yang, P., Zhang, W., 2016. Investigation of atmospheric effects on retrieval of sun-induced fluorescence using hyperspectral imagery. Sensors 16, 480.

Nichol, C.J., Drolet, G., Porcar-Castell, A., Wade, T., Sabater, N., Middleton, E.M., Maclellan, C., Levula, J., Mammarella, I., Vesala, T., Atherton, J., 2019. Diurnal and seasonal solar induced chlorophyll fluorescence and photosynthesis in a boreal scots pine canopy. Remote Sens. 11, 273.

Panigada, C., Rossini, M., Meroni, M., Cilia, C., Busetto, L., Amaducci, S., Boschetti, M., Cogliati, S., Picchi, V., Pinto, F., Marchesi, A., Colombo, R., 2014. Fluorescence, PRI and canopy temperature for water stress detection in cereal crops. Int. J. Appl. Earth Obs. Geoinf. 30, 167–178.

Headwall Photonics, 2023. HyperSpec Solar-Induced Fluorescence Imaging Sensor. URL: https://headwallphotonics.sharefile.com/share/view/s3450bb7a6f4e4f5a8a2083ebe2d564a7 [Online; accessed 25. Oct. 2023].

Plascyk, J.A., 1975. The MK II Fraunhofer line discriminator (FLD-II) for airborne and orbital remote sensing of solar-stimulated luminescence. Opt. Eng. 14, 144339.

Poblete, T., Camino, C., Beck, P.S.A., Hornero, A., Kattenborn, T., Saponari, M., Boscia, D., Navas-Cortes, J.A., Zarco-Tejada, P.J., 2020. Detection of Xylella fastidiosa infection symptoms with airborne multispectral and thermal imagery: Assessing bandset reduction performance from hyperspectral analysis. ISPRS J. Photogramm. Remote Sens. 162, 27–40.

Poblete, T., Navas-Cortes, J.A., Camino, C., Calderon, R., Hornero, A., Gonzalez-Dugo, V., Landa, B.B., Zarco-Tejada, P.J., 2021. Discriminating Xylella fastidiosa from Verticillium dahliae infections in olive trees using thermal- and hyperspectral-based plant traits. ISPRS J. Photogramm. Remote Sens. 179, 133–144.

Porcar-Castell, A., Tyystjärvi, E., Atherton, J., Van der Tol, C., Flexas, J., Pfündel, E.E., Moreno, J., Frankenberg, C., Berry, J.A., 2014. Linking chlorophyll a fluorescence to photosynthesis for remote sensing applications: mechanisms and challenges. J. Exp. Bot. 65, 4065–4095.

Rascher, U., Alonso, L., Burkart, A., Cilia, C., Cogliati, S., Colombo, R., Damm, A., Drusch, M., Guanter, L., Hanus, J., Hyvärinen, T., Julitta, T., Jussila, J., Kataja, K., Kokkalis, P., Kraft, S., Kraska, T., Matveeva, M., Moreno, J., Muller, O., Panigada, C., Pikl, M., Pinto, F., Prey, L., Pude, R., Rossini, M., Schickling, A., Schurr, U., Schüttemeyer, D., Verrelst, J., Zemek, F., 2015. Sun-induced fluorescence - a new probe of photosynthesis: first maps from the imaging spectrometer HyPlant. Glob. Chang. Biol. 21, 4673–4684.

Romero, J.M., Cordon, G.B., Lagorio, M.G., 2020. Re-absorption and scattering of chlorophyll fluorescence in canopies: A revised approach. Remote Sens. Environ. 246, 111860.

Scodellaro, R., Cesana, I., D'Alfonso, L., Bouzin, M., Collini, M., Chirico, G., Colombo, R., Miglietta, F., Celesti, M., Schuettemeyer, D., Cogliati, S., Sironi, L., 2022. A novel hybrid machine learning phasor-based approach to retrieve a full set of solar-induced fluorescence metrics and biophysical parameters. Remote Sens. Environ. 280, 113196.

Specim, 2022. AISA IBIS Fluorescence Imager. URL: https://www.adept.net.au/cameras/specim/systems/pdf/AisaIBIS.pdf [Online; accessed 25. Oct. 2023].

Suarez, L., Gonzalez-Dugo, V., Camino, C., Hornero, A., Zarco-Tejada, P.J., 2021. Physical model inversion of the green spectral region to track assimilation rate in almond trees with an airborne nano-hyperspectral imager. Remote Sens. Environ. 252 (112147), 3.

Sun, Y., Frankenberg, A., Jung, M., Joiner, J., Guanter, L., Köhler, P., Magney, T.S., 2018. Overview of solar-induced chlorophyll fluorescence (SIF) from the orbiting carbon observatory-2: retrieval, cross-mission comparison, and global monitoring for GPP. Remote Sens. Environ. 209, 808–823.

Van der Tol, C., Verhoef, W., Timmermans, J., Verhoef, A., Su, Z., 2009. An integrated model of soil-canopy spectral radiances, photosynthesis, fluorescence, temperature and energy balance. Biogeosci. 6, 3109–3129.

Van der Tol, C., Berry, J.A., Campbell, P.K.E., Rascher, U., 2014. Models of fluorescence and photosynthesis for interpreting measurements of solar-induced chlorophyll fluorescence. J. Geophys. Res. Biogeosci. 119, 2312–2327.

Van der Tol, C., Rossini, M., Cogliati, S., Verhoef, W., Colombo, R., Rascher, U., Mohammed, G., 2016. A model and measurement comparison of diurnal cycles of sun-induced chlorophyll fluorescence of crops. Remote Sens. Environ. 186, 663–677.

Van der Tol, C., Vilfan, N., Dauwe, D., Cendrero-Mateo, M.P., Yang, P., 2019. The scattering and re-absorption of red and near-infrared chlorophyll fluorescence in the models Fluspect and SCOPE. Remote Sens. Environ. 232, 111292.

Verhoef, W., van der Tol, C., Middleton, E.M., 2018. Hyperspectral radiative transfer modeling to explore the combined retrieval of biophysical parameters and canopy fluorescence from FLEX – Sentinel-3 tandem mission multi-sensor data. Remote Sens. Environ. 204, 942–963.

Verhoef, W., 1998. Theory of Radiative Transfer Models Applied in Optical Remote Sensing of Vegetation Canopies (PhD thesis). Wageningen University ISBN 90-5485-804-4.

Verrelst, J., Rivera, J.P., Van der Tol, C., Magnani, F., Mohammed, G., Moreno, J., 2015. Global sensitivity analysis of the SCOPE model: what drives simulated canopy-leaving sun-induced fluorescence? Remote Sens. Environ. 166, 8–21.

Wang, R., Gamon, J.A., Hmimina, G., Cogliati, S., Zygielbaum, A.I., Arkebauer, T.J., Suyker, A., 2022a. Harmonizing solar induced fluorescence across spatial scales, instruments, and extraction methods using proximal and airborne remote sensing: A multi-scale study in a soybean field. Remote Sens. Environ. 281, 113268.

Wang, Y., Suarez, L., Poblete, T., Gonzalez-Dugo, V., Ryu, D., Zarco-Tejada, P.J., 2022b. Evaluating the role of solar-induced fluorescence (SIF) and plant physiological traits for leaf nitrogen assessment in almond using airborne hyperspectral imagery. Remote Sens. Environ. 279, 113141.

Wang, N., Suomalainen, J., Bartholomeus, H., Kooistra, L., Masiliūnas, D., Clevers, J.G.P. W., 2021. Diurnal variation of sun-induced chlorophyll fluorescence of agricultural crops observed from a point-based spectrometer on a UAV. Int. J. Appl. Earth Obs. Geoinf. 96, 102276.

Wang, N., Yang, P., Clevers, J.G., Wieneke, S., Kooistra, L., 2023. Decoupling physiological and non-physiological responses of sugar beet to water stress from sun-induced chlorophyll fluorescence. Remote Sens. Environ. 286, 113445.

Watt, M.S., Buddenbaum, H., Leonardo, E.M.C., Estarija, H.J.C., Bown, H.E., Gomez-Gallego, M., Hartley, R., Massam, P., Wright, L., Zarco-Tejada, P.J., 2020. Using hyperspectral plant traits linked to photosynthetic efficiency to assess N and P partition. ISPRS J. Photogramm. Remote Sens. 169, 406–420.

Wieneke, S., Pacheco-Labrador, J., Mahecha, M.D., Poblador, S., Vicca, S., Janssens, I.A., 2024. Comparing the quantum use efficiency of red and far-red sun-induced fluorescence at leaf and canopy under heat-drought stress. Remote Sens. Environ. 311, 114294.

Wu, L., Zhang, Y., Zhang, Z., Zhang, X., Wu, Y., Chen, J.M., 2024. Deriving photosystem-level red chlorophyll fluorescence emission by combining leaf chlorophyll content and canopy far-red solar-induced fluorescence: Possibilities and challenges. Remote Sens. Environ. 304, 114043.

Yang, P., Van der Tol, C., Verhoef, W., Damm, A., Schickling, A., Kraska, T., Muller, O., Rascher, U., 2019. Using reflectance to explain vegetation biochemical and structural effects on sun-induced chlorophyll fluorescence. Remote Sens. Environ. 231, 110996.

Yang, P., Prikaziuk, E., Verhoef, W., Van der Tol, C., 2021. SCOPE 2.0: A model to simulate vegetated land surface fluxes and satellite signals. Geosci. Model Dev. 14, 4697–4712.

Yang, P., Van der Tol, C., 2018. Linking canopy scattering of far-red sun-induced chlorophyll fluorescence with reflectance. Remote Sens. Environ. 209, 456–467.

Zarco-Tejada, P.J., González-Dugo, V., Berni, J.A.J., 2012. Fluorescence, temperature and narrow-band indices acquired from a UAV platform for water stress detection using a micro-hyperspectral imager and a thermal camera. Remote Sens. Environ. 117, 322–337.

Zarco-Tejada, P.J., Morales, A., Testi, L., Villalobos, F.J., 2013. Spatio-temporal patterns of chlorophyll fluorescence and physiological and structural indices acquired from hyperspectral imagery as compared with carbon fluxes measured with eddy covariance. Remote Sens. Environ. 133, 102–115.

Zarco-Tejada, P.J., González-Dugo, M.V., Fereres, E., 2016. Seasonal stability of chlorophyll fluorescence quantified from airborne hyperspectral imagery as an indicator of net photosynthesis in the context of precision agriculture. Remote Sens. Environ. 179, 89–103.

Zarco-Tejada, P.J., Camino, C., Beck, P.S.A., Calderon, R., Hornero, A., Hernández-Clemente, R., Kattenborn, T., Montes-Borrego, M., Susca, L., Morelli, M., Gonzalez-Dugo, V., North, P.R.J., Landa, B.B., Boscia, D., Saponari, M., Navas-Cortes, J.A., 2018. Previsual symptoms of Xylella fastidiosa infection revealed in spectral plant-trait alterations. Nat. Plants 4, 432–439.

Zarco-Tejada, P.J., Poblete, T., Camino, C., Gonzalez-Dugo, V., Calderon, R., Hornero, A., Hernández-Clemente, R., Román-Écija, M., Velasco-Amo, M.P., Landa, B.B., Beck, P. S.A., Saponari, M., Boscia, D., Navas-Cortes, J.A., 2021. Divergent abiotic spectral pathways unravel pathogen stress signals across species. Nat. Commun. 12, 6088.

Zeng, Y., Badgley, G., Dechant, B., Ryu, Y., Chen, M., Berry, J.A., 2019. A practical approach for estimating the escape ratio of solar-induced chlorophyll fluorescence. Remote Sens. Environ. 232, 111209.

Zeng, Y., Chen, M., Hao, D., Damm, A., Badgley, G., Rascher, U., Johnson, J.E., Dechant, B., Siegmann, B., Ryu, Y., Qiu, H., 2022. Combining near-infrared radiance of vegetation and fluorescence spectroscopy to detect effects of abiotic changes and stresses. Remote Sens. Environ. 270, 112856.

Zhao, F., Dai, X., Verhoef, W., Guo, Y., Van der Tol, C., Li, Y., Huang, Y., 2016. FluorWPS: a Monte Carlo ray-tracing model to compute sun-induced chlorophyll fluorescence of three-dimensional canopy. Remote Sens. Environ. 187, 385–399.